nature communications

Article

https://doi.org/10.1038/s41467-025-67263-w

TIGIT disruption rescues the antitumor activity of low avidity TCR-engineered T cells by increasing TCR signal strength

Received: 15 April 2025

Accepted: 26 November 2025

Martina Spiga[1,15], **Alessia Potenza**[1,15], **Zulma Magnani**[1], **Stefano Beretta**[2], **Barbara Camisa**[1], **Laura Conte**[1], **Alessia Airaghi**[1], **Neda Mohammadi**[1], **Laura Perani**[3], **Claudio Doglioni**[4,5], **Maurilio Ponzoni**[4,5], **Francesca Sanvito**[4], **Chiara Balestrieri**[1,6], **Lucia Sergi Sergi**[1], **Oronza A. Botrugno**[5,7], **Giulio Giovannoni**[7], **Giovanni Tonon**[5,6,7], **Danilo Abbati**[1], **Chiara Iozzi**[1], **Maximilian Reichert**[8], **Hana Algul**[9], **Arianna Pocaterra**[10], **Martina Fiumara**[2], **Samuele Ferrari**[2,5], **Alessia Ugolini**[1], **Alice Grometto**[1], **Giulia Di Lullo**[1], **Giovanni Sitia**[5,11], **Giulio Belfiori**[12], **Maria Pia Protti**[13], **Renato Ostuni**[2,5], **Anna Mondino**[10], **Michele Reni**[5,14], **Stefano Crippa**[5,12], **Massimo Falconi**[5,12], **Luigi Naldini**[2,5], **Eliana Ruggiero**[1,16] & **Chiara Bonini**[1,5,16] ✉

T-cell avidity is a major determinant of Adoptive T cell therapy (ACT) efficacy for cancer treatment. However, high-avidity tumor-specific T cells can rarely be isolated from cancer patients, highlighting the need for strategies to enhance the cytotoxic capacity of low-avidity cells. Here, we rescue the antitumor functions of low-avidity T cells against pancreatic ductal adenocarcinoma (PDAC) by knocking-out TIGIT, a key inhibitory molecule expressed on exhausted CD8$^+$ T cells infiltrating gastrointestinal tumors. We uncover that TIGIT disruption by base editing boosts the intracellular signal transduction derived from a weak T cell receptor (TCR) engagement enforcing cytoskeletal rearrangements, thus increasing T cell avidity and stabilizing the immunological synapse. Accordingly, TIGIT disruption enables low-avidity T cells to exert robust degranulation, comparable to that of high-avidity T cells, and potent and durable anti-tumor capacity in vivo in male mice. These results highlight TIGIT knockout as a potential strategy to enhance low-avidity T cell function and broaden the repertoire of TCR engineered T cells in the treatment of pancreatic cancer and other solid malignancies.

While Adoptive T Cell Therapy (ACT) revolutionized the treatment of hematological malignancies, its efficacy in solid tumors remains suboptimal[1]. A key limitation is the identification of functional TCRs specific for relevant tumor antigens, especially in tumors with low mutational burden. Several protocols have been now developed to isolate tumor-specific TCRs from either patients or healthy donors; however, clones that are highly reactive against tumor-associated antigens (TAAs), which are self-antigens highly overexpressed by cancer cells and shared across patients, are scarce. This heightens the probability of isolating low-avidity T cell populations, demonstrated to be less effective in building a sufficient immune response for promoting tumor shrinkage[2,3]. Hence, innovative strategies to enhance the

A full list of affiliations appears at the end of the paper. ✉e-mail: bonini.chiara@hsr.it

functionality of low-avidity T cells, are required to broaden the applicability of T cell transfer and to deliver safe and effective products to patients diagnosed with solid tumors. Among these, pancreatic ductal adenocarcinoma (PDAC) is predicted to become the second leading cause of cancer-related death within the next 10 years, surpassing colorectal cancer[4]. Advanced patients represent the majority (80-85%) of PDAC diagnoses, precipitating the 5-year survival rate to 8%[5], and their outcome is poorly impacted by conventional treatments or immunotherapy with immune checkpoint blockade[6]. This is due to the intrinsic aggressiveness of this tumor entity, sustained by networks of malignant and non-malignant cells that build strong immunosuppressive interactions and an immune-excluded tumor microenvironment[4]. Accordingly, although neoantigen vaccines can delay PDAC relapse in a consistent proportion of patients, this is achieved mainly by priming of new T cell responses rather than by boosting pre-existing tumor-specific T cells in tumor lesions[7,8]. Thus, T cell therapy in PDAC is theoretically feasible but likely limited by the absence and the inability to isolate good T cell clones. As observed in other solid tumors, tumor reactive T cells isolated from PDAC patients are exhausted and dysfunctional[9,10]. The possibility to transfer tumor-specific TCRs to healthy T cells[11–14] allows to overcome several of these hurdles, but not the low affinity of the TCR itself. With the aim of developing an ACT strategy to treat patients with PDAC, in this study we applied our pipeline to isolate novel TCRs specific for relevant tumor antigens and widened their exploitability by harnessing the co-inhibitory receptor TIGIT. TIGIT associates with the TCR at the immunological synapse[15] and inhibits T cell activation through cell-intrinsic and -extrinsic mechanisms, including interfering with CD226 stimulatory signals and inducing tolerogenic dendritic cells[16]. An increased TIGIT expression has been observed in T cells upon chronic antigen exposure during viral infections and cancer[17], promoting immune evasion. In PDAC, TIGIT ligands have been found upregulated both on tumor cells and antigen-presenting cells[18], and TIGIT expression is enriched on tumor-infiltrating CD8$^+$ T cells correlating with exhaustion features[9,19–22].

Despite TIGIT blockade with monoclonal antibodies gained traction in the clinic, recent trials reported mild (NCT04524871, NCT04524871, NCT02964013, CITYSCAPE trial) or no (SKYSCRAPER trial, KeyVibe trials) effects on ameliorating progression-free and overall survival, with concomitant manifestations of immune-related adverse events such as lipase increase and infections when delivered both as mono- and combined therapy[23,24]. This highlights the need for a selective strategy to target TIGIT in T cells. We reasoned that the genetic disruption of TIGIT in TCR-engineered T cells could increase the efficacy and specificity of this therapeutic approach, and further help in shedding light on the mechanisms underlying TIGIT function. Here, we demonstrate how base editing-mediated TIGIT gene disruption enables low-avidity T cells to exert potent anti-tumor activity against PDAC and other gastrointestinal tumors, and associate this functional boosting with increased TCR signal strength, enhanced T cell avidity and improved establishment of the immunological synapse between T cells and tumor cells.

Results

TCR-engineered T cells targeting PDAC exhibit a wide range of avidity

To select relevant antigens for engineered T cells, we designed a computational workflow (Supplementary Fig. 1A). We prioritized antigens frequently overexpressed in PDAC, focusing on those with well-established roles in tumorigenesis and reported as immunogenic, ending up with 19 TAAs and 1 neoantigen. By TCR hunting[13,14], from one healthy donor and one PDAC patient (see “Methods”), we isolated 4 and 1 HLA-A*0201-restricted TCRs, respectively, targeting AGR2[25], DKK1[26], MET[27], MSLN[28] and MUC5AC[29] (Supplementary Fig. 1B–D, Supplementary Fig. 2). All targeted antigens are highly expressed in PDAC lesions and mostly maintained during disease progression, as observed by RNAseq[30] data reported from primary PDAC and liver metastases (Fig. 1A) and confirmed by immunohistochemistry on our samples (Fig. 1B). We evaluated TAA expression levels in healthy tissues, combining RNAseq data from the Genotype-Tissue Expression (GTEx) database and protein expression by immunohistochemistry on healthy tissue biopsies from our biobank. We observed that while AGR2 and MET are broadly expressed in the urinal, gastrointestinal, and respiratory tracts, and MUC5AC transcript is highly present in the stomach mucosa, both MSLN and DKK1 exhibit minimal expression in healthy tissues (Fig. 1C). To exploit the newly identified tumor-specific TCRs for cell therapy, we coupled base editing with lentiviral vector (LV) delivery to generate TCR gene edited T cells (Fig. 1D). Specifically, to disrupt the endogenous TCR[11–13,31–33] we compared BE4max cytosine base editor (CBE) and ABE8.20 m adenine base editor (ABE)[34]. We tested 2 single guide RNAs (sgRNAs) directed toward *TRAC*[35] and designed 5 sgRNAs targeting *TRBC* (Supplementary Fig 3A). By ranking sgRNAs (sg) in terms of editing efficiencies, measured as loss of CD3 surface expression[11], we selected TRAC sg2 and TRBC1/2 sg5 as the most effective sgRNAs and BE4max for further exploitation (Supplementary Fig 3B, C). We thus generated CD3^{neg} T cells by simultaneously disrupting *TRAC*, *TRBC1*, and *TRBC2*, achieving a mean target base conversion of 82.5% (range: 67–100%) for *TRAC*, 66.2% (range: 47–92%) for *TRBC1*, and 55.7% (range: 43–70%) for *TRBC2*, with an overall 96% frequency of TCR disruption quantified by CD3 surface abundance (Fig. 1E). We then redirected T cell specificity by transducing CD3^{neg} T cells with bidirectional LVs, each encoding for 1 TAA-specific TCR (Supplementary Fig. 3D), obtaining a restoration of CD3 surface expression above 70% for most TCR constructs, which was associated with the expression of the TAA-specific TCR (Fig. 1F). To evaluate the TCR specificities, we challenged TCR-edited T cells with PDAC cells for 24 h and observed a comparable tumor killing efficacy (approx. 43% killing) among T cell products, with MSLN-specific T cells being the most cytolytic. Of note, all TCR-edited T cells spared HLA-A*02:01$^+$ antigen^{neg} and HLA-A*02:01^{neg} cell lines, demonstrating recognition specificity (Fig. 2A). Being avidity a major determinant and a predictive biomarker of T cell efficacy in vivo[2,3,36–39], we measured and compared the avidity of our TCR-edited T cells by Z-Movi, which tests the strength of interactions between T cells and target cells[36,37,39]. To minimize biases derived from antigen expression levels, we used K562-A2$^+$ cell lines pulsed with the cognate TCR peptides (i.e P1, P9, P17, P23, P35, Supplementary Fig. 1B–D) as target cells. After letting CD8$^+$ TCR-edited T cells react for 5 min, we observed them distributing among two avidity classes, with AGR2-, DKK1- and MUC5AC-specific T cells displaying the strongest target binding, while MSLN- and MET-specific T cells generate the weakest interactions (Fig. 2B). Overall, although our 5 cellular products proved equally efficient in killing antigen bearing targets in vitro, only DKK1 and MSLN-specific cells displayed the most favorable specificity profile and were thus selected for further studies. Of notice, while DKK1 specific cells are high avidity, the avidity of MSLN specific T lymphocytes proved suboptimal.

To verify the functional relevance of T cell avidity, we challenged DKK1 and MSLN-redirected T cells with HLA-A*02:01$^+$ T2 cells pulsed with diluting concentrations of the target epitopes and measured pro-inflammatory cytokines production, i.e IFNγ, IL-2, and TNFα, and degranulation capacity (CD107a). In accordance with their avidity, T cells targeting DKK1 present more polyfunctional than MSLN-specific cells, as indicated by the co-expression of up to two different pro-inflammatory molecules at limited peptide concentrations (Fig. 2C, D). Thus, from the original 5 receptors, we ended up with only 1 viable T cell product.

Rescuing low avidity T cells by TIGIT disruption

Considering the need for a wide range of tumor-reactive T cells to ensure anti-tumor efficacy and to reduce the risk of cancer immune

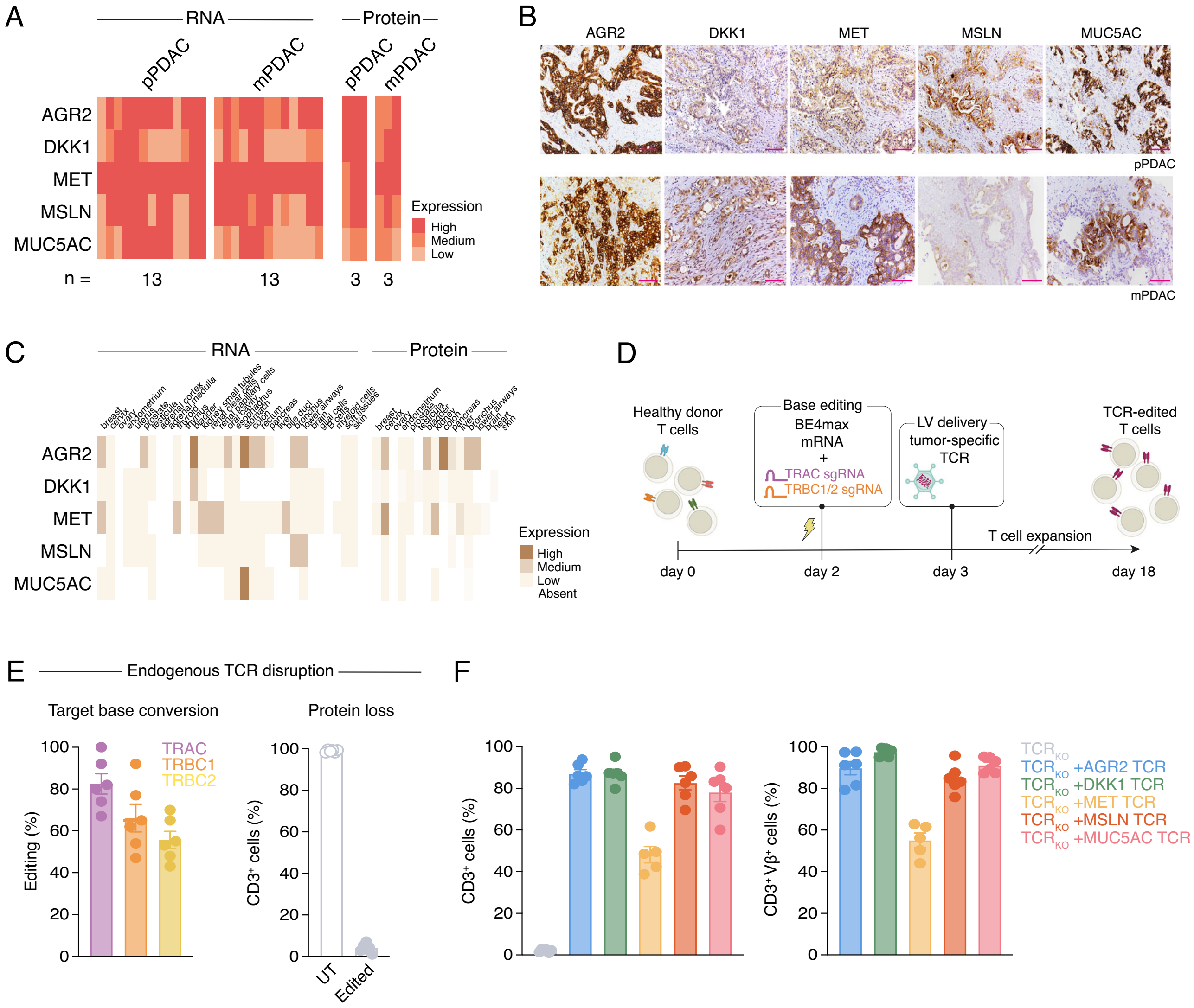

Fig. 1 | Engineering T cells toward PDAC TAAs via base editing and LV delivery of tumor-specific TCRs. A Heatmap depicting transcriptional and protein levels of target TAAs measured in primary PDAC samples (pPDAC) and in liver metastases (mPDAC). Numbers of samples analyzed are shown for each tumor type.
B Representative immunohistochemistry images of target antigen expression in PDAC primary tumor sample (top) and liver metastasis (bottom). Scale bar 100 µm. Each experiment was repeated independently on three different biological samples. **C** Heatmap representing transcriptional and protein antigen expression in healthy tissues. Transcript expression data were retrieved from GTEx database using GEPIA2.0. Protein expression was quantified by immunohistochemistry. $N = 1$–3 for each tissue. **D** Workflow for the generation of TCR_{KO} TAAs-redirected T cells. **E** Simultaneous editing efficiency of the endogenous TCR by BE4max evaluated at the genomic level as frequency of C•G-to-T•A conversion at the target base in *TRAC*, *TRBC1* and *TRBC2* (left) and at the protein level, measured as loss of CD3 surface expression compared to untreated T cells (right). $N = 6$ biological independent samples. **F** TAA-TCRs transduction efficiency in TCR_{KO} T cells measured as CD3 surface re-expression (left) and expression of the TCR Vβ family for each TAA-TCR (right). $N = 6$ biological independent samples for UT and AGR2, DKK1, MSLN and MUC5AC TCRs; $N = 5$ for MET TCR. Data are represented as mean ± s.e.m. Source data and exact p values are provided as a Source Data file.

evasion[40–43], and that most tumor-specific TCRs targeting TAAs display low avidity[3,44], we verified whether additional genetic manipulation could rescue the anti-tumor potential of low-avidity cells. We hypothesized that genetic disruption of the co-inhibitory receptor TIGIT, which upregulation has been often observed in exhausted T cells infiltrating solid tumors[17] including PDAC, could rescue the functional avidity of MSLN-redirected T cells. Upon binding with its ligand CD155, TIGIT clusters with the TCR at the immunological synapse[15,45]. We thus postulated that TIGIT deletion could foster TCR signaling propagation and, by that, improve the reactivity of low-avidity T cells. We designed 5 sgRNAs targeting *TIGIT* to couple its disruption with the TCR base editing protocol, ending up selecting sg4 for its high frequency of target base conversion, which resulted in TIGIT surface loss (Supplementary Fig. 4A–C). The simultaneous targeting of *TRAC*, *TRBC1/2*, and *TIGIT* (Supplementary Fig. 4D) by BE4max resulted in a mean disruption efficiency of 96.8% (range: 89–100%) for *TRAC*, 62% (range: 46–81%) for *TRBC1*, 47.5% (range: 35–57%) for *TRBC2* and 81.5% (range: 66–100%) for *TIGIT*, producing T cells deprived of the surface expression of both the endogenous TCR and TIGIT (Fig. 2E). We redirected the specificity of TCR knockout TIGIT knockout ($TCR_{KO}TIGIT_{KO}$) and TCR knockout TIGIT competent ($TCR_{KO}TIGIT_{COMP}$) T cells by lentiviral transduction and monitored the T cell culture for 15-18 days. Importantly, we observed that TIGIT knockout is not affecting T cell expansion capacity nor the maintenance of an early-memory phenotype in the engineered T cell products (Fig. 2F, Supplementary Fig. 4E). Next, we evaluated the impact of TIGIT disruption on T cell avidity. Surprisingly, we observed that TIGIT disruption increases the avidity of low-avidity MSLN-specific T cells, while mediating no effect on high-avidity DKK1-specific lymphocytes (Fig. 2G). Consistently, while IL-2 secretion was not

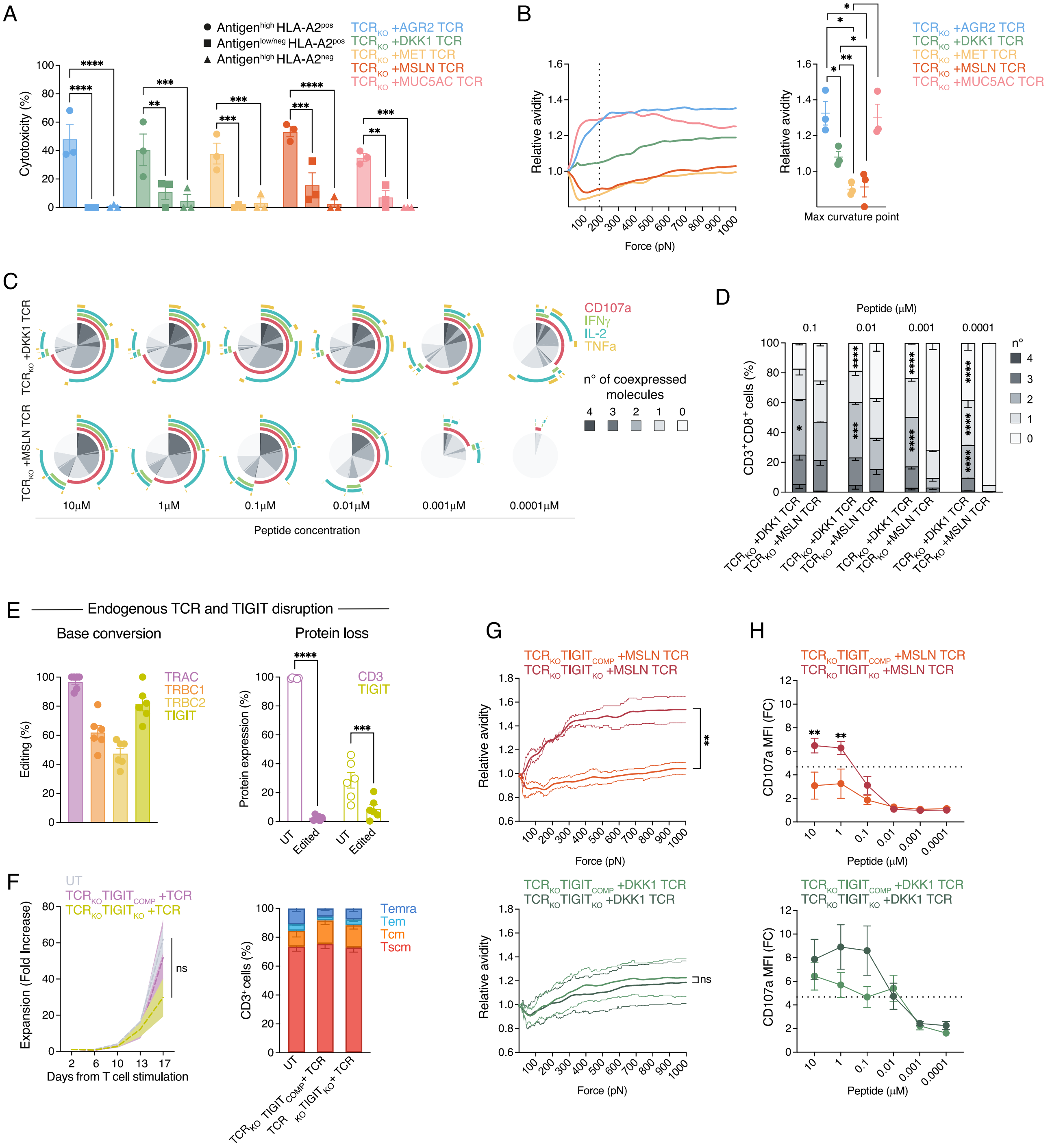

influenced by TIGIT manipulation (Supplementary Fig. 5A), we observed an improved degranulation capacity in TIGIT_{KO} vs $\text{TIGIT}_{\text{COMP}}$ MSLN-specific T cells, but not in high-avidity DKK1-specific T cells (Fig. 2H). Overall, we found that disrupting TIGIT in low-avidity T cells enhances their avidity and restores their cytotoxic functions.

TIGIT disruption enhances the TCR signal strength of low avidity T cells

To gain deeper insights into the molecular mechanisms associated with TIGIT knockout effects in low-, but not high-, avidity T cells, we used phospho-flow cytometry to reveal the activation of a subset of signaling elements downstream TCR engagement. Indeed, TCR levels were similar in $\text{TCR}_{\text{KO}}\text{TIGIT}_{\text{COMP}}$ and $\text{TCR}_{\text{KO}}\text{TIGIT}_{\text{KO}}$ T cells independently from the transgenic TCR used and transduction efficiencies (Supplementary Fig. 5B, C). Moreover, CD3 surface levels, used as proxy for proper TCR signaling engagement, was similarly downregulated upon antigen encounter (Fig. 3A, S5D), supporting the notion that TIGIT disruption affects T cell activation downstream the TCR/CD3 complex. Upon coculture of low-avidity MSLN-specific T cells with MSLN-pulsed K562-A2$^+$, we observed an increase in the phosphorylation of ZAP70, but not of ERK1/2 or S6, in TIGIT_{KO} compared to $\text{TIGIT}_{\text{COMP}}$ cells (Fig. 3B). On the other hand, in high-avidity DKK1-specific effectors, the phosphorylation of ZAP70 and ERK1/2, was unaffected by TIGIT knockout (Supplementary Fig. 5E). Thus, TIGIT deletion improves the TCR signal strength only when T cell activation is conveyed to low-avidity T cells.

Fig. 2 | TIGIT disruption increases T cell avidity and recover degranulation capacity of low-avidity T cells. A Killing capacity of TAA-TCR edited T cells cocultured at 5:1 effector-to-target ratio with BxPC3-A2+ (antigen positive, HLA-A*0201 positive) PDAC cell line. Antigen low/negative or HLA-A*0201 negative cell lines were used as controls. $N = 3$ biological independent samples for each TCR. **B** Avidity of TAA-TCR edited T cells on K562-A2+ leukemic cell line pulsed with 10 µg/ml of each specific peptide (left). Statistical analysis was performed on the max curvature point of AGR2 avidity curve (dotted line, right). $N = 3$ matched biological independent samples for each TCR. Statistical analysis by paired two-tailed t test. **C**, **D** Functional avidity of TCR_{KO} DKK1- and MSLN-specific T cells indicated as the co-expression of CD107a, IFNγ, IL-2, and TNFα after a 6 h co-culture with T2 cells loaded with decreasing concentrations of each specific peptide or an unrelated one as control. n°(0-4) indicates the number of co-expressed molecules. $N = 3$ biological independent samples for MSLN-specific T cells, $n = 2$ biological independent samples for DKK1-specific T cells. **E** Simultaneous editing efficiency of the endogenous TCR and TIGIT by BE4max evaluated at day 15 after T cell activation. Editing efficiency is indicated as frequency of C•G-to-T•A conversion at the target base in *TRAC*, *TRBC1*, *TRBC2* and *TIGIT* (left) and as reduction of CD3 and TIGIT surface expression in multiplex edited T cells (edited) compared to untreated T cells (UT, right). $N = 6$ biological independent samples. **F** Expansion of total viable $TCR_{KO}TIGIT_{KO}$ + TCR and $TCR_{KO}TIGIT_{COMP}$ + TCR T cells. Untreated T cells were used as control (left). $N = 3$ matched biological independent samples. Relative distribution of stem memory (T_{SCM}; $CD45RA^+CD62L^+$), central memory (T_{CM}; $CD45RA^-CD62L^+$), effector memory (T_{EM}; $CD45RA^-CD62L^-$), and terminally differentiated effector (T_{EMRA}; $CD45RA^+CD62L^-$) cells for each T cell group (right). $N = 6$ matched biological independent samples. **G** Avidity of $TCR_{KO}TIGIT_{KO}$ and $TCR_{KO}TIGIT_{COMP}$ MSLN-specific T cells (top) and DKK1-specific T cells (bottom) measured as in (**B**). $N = 2$ biological independent samples for MSLN-specific T cells, $n = 3$ biological independent samples for DKK1-specific T cells. Statistical analysis by paired two-tailed t-test. **H** Functional avidity of $TCR_{KO}TIGIT_{KO}$ and $TCR_{KO}TIGIT_{COMP}$ MSLN-specific T cells (top) and DKK1-specific T cells (bottom) measured as in (**C**, **D**). The dotted line represents the smallest significant value of $TCR_{KO}TIGIT_{COMP}$ DKK1-specific T cells when compared to its control. $N = 3$ biological independent samples for each TCR specificity. Data are represented as mean ± s.e.m. Statistical analysis performed by two-way ANOVA unless otherwise stated. *, $P < 0.05$; **, $P < 0.01$; ***, $P < 0.001$; ****, $P < 0.0001$. Source data and exact p values are provided as a Source Data file.

At the intracellular level, while the phosphorylation of ZAP70 is a specific feature of the TCR-peptide MHC interaction[46], the costimulatory cues converge with the TCR signal within the Ras/ERK and the AKT/mTOR signaling pathways[47,48] (Supplementary Fig. 5F). Of note, when the same experiment was performed in the presence of CD28-mediated co-stimulation, both high- and low-avidity $TIGIT_{KO}$ cellular products displayed enhanced phosphorylation of ERK1/2 (Fig. 3C, Supplementary Fig. 5G), indicating that TIGIT expression can also influence T cell co-stimulation, and that this effect is independent from the TCR strength. Finally, the TCR and costimulatory molecules downstream signaling lead to the regulation of actin dynamic, which is essential to stabilize the interaction between T and target cells[49–51]. Indeed, upon exposure of MSLN-specific T cells to patient-derived tumor organoids (PDOs), we observed that $TIGIT_{KO}$ cells display an increased actin polymerization (Fig. 3D) and a 2.9-fold increase in the frequency of immunological synapses between T cells and target cells, compared to $TIGIT_{COMP}$ lymphocytes (Fig. 3E). Consistently with an enhanced T cell activation, we detected an increased expression of PD1 24 h after antigen encounter in $TIGIT_{KO}$ MSLN-specific T cells compared to DKK1-specific ones, which was not associated to LAG3 nor TIM3 upregulation (Fig. 3F, S5H). Beyond its capacity to suppress T cells by TCR-proximal signaling[15], TIGIT has been extensively characterized for inhibiting DNAM1, which is both a costimulatory and a non-conventional adhesion molecule playing a major role in the interaction of T cells with tumor cells[52–57]. Interestingly, we observed that while the frequency of DNAM1 positive cells remained unaltered, DNAM1 expression levels decreased upon both TCR-independent and -dependent T cell activation (Fig. 3G). However, TIGIT knockout sustained DNAM1 downregulation in MSLN-specific but not in DKK1-specific T cells. Accordingly, $TIGIT_{KO}$ MSLN-specific T cells displayed a better proliferative capacity than $TIGIT_{COMP}$ counterparts, and similar to that of $TIGIT_{KO}$ and $TIGIT_{COMP}$ DKK1 effectors (Fig. 3H, I).

In tumor-infiltrating lymphocytes, TIGIT blockade restores their cytotoxic capacity by improving glucose metabolism[58,59]. Thus, to verify whether the functional advantage of TIGIT disruption in low-avidity T cells, is related to a shift in the glycolytic metabolism, we measured glucose uptake but observed no difference between $TIGIT_{COMP}$ and $TIGIT_{KO}$ MSLN- and DKK1-redirected T cells. (Supplementary Fig. 5I).

All together, these data show that TIGIT gene disruption boosts the activation of low-avidity TCR-engineered T cells by increasing ZAP70 phosphorylation and sustaining DNAM1 engagement, which ultimately enforces the stabilization of the immunological synapse with cancer cells (Fig. 3J).

Safety of base editing to generate $TCR_{KO}TIGIT_{KO}$ T cells

Even though CBE are currently employed in clinical applications[32], an extensive evaluation of the off-target events resulting from CBE usage in T cells is still missing. The potential DNA off-target deamination has been mainly associated with the activity of cytosine base editors[60,61], as BE4max, and represents a relevant safety concern when targeting multiple genes. We thus measured and compared off-target events occurring in $TCR_{KO}TIGIT_{KO}$ T cells edited with BE4max, to those observed in mock electroporated (untreated) T cells as controls (Fig. 4A). First, we ensured that bystander editing, mediated by BE4max and occurring at non-target cytosines located within the editing window (3-11 bases of the sgRNA targets), mostly caused silent mutations and were not affecting T cell fitness (Supplementary Fig. 6A, B). Then, to measure sgRNA-dependent off-target events, we sequenced 8 predicted off-target *loci* mapping on coding regions (Supplementary Fig. 7A) and confirmed high on-target editing efficiency in the absence of off-target base conversions (Fig. 4B). To quantify putative sgRNA-independent off-target editing, we performed ultra-deep whole exome sequencing (WES) of base-edited ($TCR_{KO}TIGIT_{KO}$) and untreated T cells generated from 4 matched healthy donors. We filtered out shared variants, which reflect germinal mutations and represent most variants detected (Supplementary Fig. 7B). By analyzing treatment-associated variants, we did not observe differences in the proportion of substitutions, deletions or insertions, or specific enrichment of transversions and transitions caused by BE4max treatment (Fig. 4C, D). By comparing edited vs untreated cells, we noticed a contraction in the absolute number of mutations detected for T cell donor 1 and 2, and a slight increase for donor 3 and donor 4, suggesting a wide donor dependance, possibly linked to a high variability in the fitness of the starting material (Supplementary Fig. 7C). Despite only few of the single nucleotide conversions were predicted to produce an impact (approx. 0.1% of total variants detected, Supplementary Fig. 7D), we decided to carefully analyze 7 gene panels bearing the potential to influence the safety and fitness of the therapeutic T cell product (Supplementary Fig. 7E). We observed a similar mutation profile in $TCR_{KO}TIGIT_{KO}$ and untreated T cells (Fig. 4E, Supplementary Fig. 7F). Importantly, of the four missense mutations observed, only one (located in MUC17, a senescence associated gene) was identified in base-edited cells (donor 2, black arrow), while the other 3 were found in untreated samples. Finally, we compared $TCR_{KO}TIGIT_{KO}$ T cells engineered through the innovative BE4max or the standard CRISPR/Cas9 genome editing tool for the presence of translocations between our four target *loci*. Despite a similar editing efficiency in multiplex setting (Supplementary Fig. 7G),

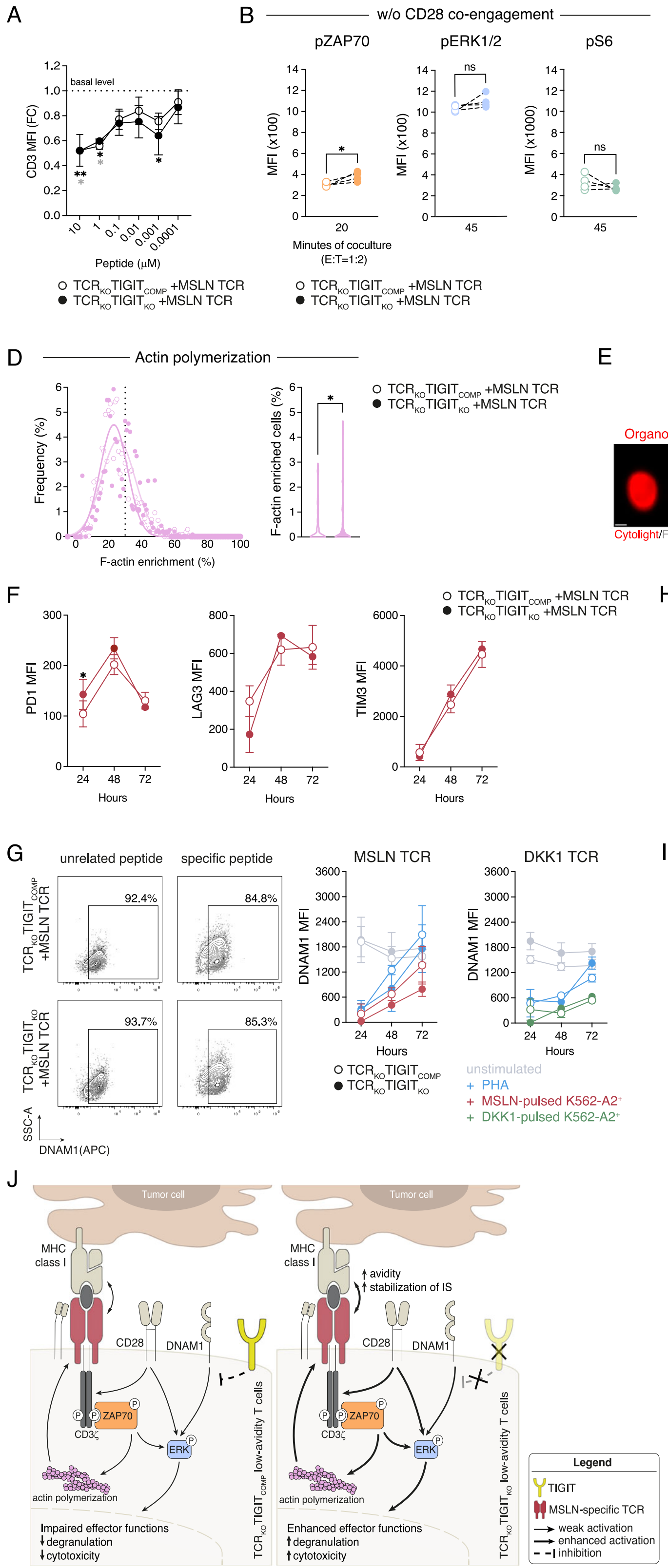

translocations were clearly detectable by ddPCR in CRISPR/Cas9, but not in BE4max edited cells (up to 0.44%, Fig. 4F).

To further corroborate the safety of our edited T cells, we tested the alloreactive (allo) and auto-reactivity of bystander products of our genetic manipulation procedure, which represent around 3% of the infused T cells and are defined as TIGIT$_{KO}$ T cells still harboring their endogenous TCR (Supplementary Fig. 8A). Importantly, upon interaction with mismatched and matched PBMCs, TIGIT knockout T cells expressing their endogenous TCR (endoTCR TIGIT$_{KO}$) showed equal allo and autoreactive potential to TIGIT competent counterparts (endoTCR TIGIT$_{COMP}$) measured by IFNγ production (Supplementary Fig. 8B) and target cell killing capacity (Supplementary Fig. 8C).

Fig. 3 | TIGIT knockout enhances TCR intracellular signaling in low-avidity T cells. A CD3 downregulation measured after a 6 h co-culture of engineered T cells with K562-A2$^+$ cells loaded with decreasing concentrations of the specific peptide or an unrelated one as control. CD3 levels are reported as ratio to its control. $N = 3$ biological independent samples, statistical analysis by two-way ANOVA. Statistical significance of $TCR_{KO}TIGIT_{KO}$ and $TCR_{KO}TIGIT_{COMP}$ against their unrelated control is reported in black and gray, respectively. **B** MFI of indicated phosphorylated markers in $TCR_{KO}TIGIT_{KO}$ and $TCR_{KO}TIGIT_{COMP}$ MSLN-specific T cells measured after 20 or 45 min coculture with K562-A2+ leukemic cell line pulsed with 10 mg/ml of MSLN specific peptide. $N = 2$ biological independent samples. Pooled data from $n = 2$ experiments. **C** MFI of indicated phosphorylated markers in $TCR_{KO}TIGIT_{KO}$ and $TCR_{KO}TIGIT_{COMP}$ MSLN-specific T cells measured by as in (**B**), with the addition of 1 mg/ml of anti-CD28 antibody. $N = 2$ biological independent samples. Pooled data from $n = 2$ experiments. **D** Distribution of T cell-cancer cell doublets relative to F-actin increase at the cell contact region for $TCR_{KO}TIGIT_{KO}$ or $TCR_{KO}TIGIT_{COMP}$ MSLN-specific T cells (left) and quantification of doublets with an F-actin enrichment >30% (right). Data were obtained by ImageStream of $TCR_{KO}TIGIT_{KO}$ MSLN-specific T cells recognizing PDOs after 45 min coculture. $N = 3$ matched biological independent samples. **E** Representative images for detection of immunological synapses (left) and frequency of immunological synapses within doublets with an F-actin enrichment >30%. $N = 3$ matched biological independent samples. Scale bar 7 µm. **F** Kinetics of PD1, LAG3, and TIM3 expression in $TCR_{KO}TIGIT_{KO}$ and $TCR_{KO}TIGIT_{COMP}$ MSLN-specific T cells upon coculture with peptide-pulsed K562-A2$^+$ cells at 1:1 effector-to-target ratio for 24, 48, and 72 h. $N = 3$ biological independent samples. **G** MFI of DNAM1 in $TCR_{KO}TIGIT_{KO}$ and $TCR_{KO}TIGIT_{COMP}$ MSLN-specific (left) and DKK1-specific (right) T cells measured as in (**F**). Unstimulated T cells and PHA-stimulated T cells were used as negative and positive control, respectively. Representative plots of DNAM$^+$ T cell frequency are shown on the left. $N = 3$ biological independent samples for each TCR specificity. **H** Kinetic of DNAM1 expression in $TCR_{KO}TIGIT_{KO}$ and $TCR_{KO}TIGIT_{COMP}$ MSLN-specific (left) as in (**G**) and frequency of proliferating T cells measured by CellTrace dilution after 72 h coculture with peptide-pulsed K562-A2$^+$ (right). $N = 3$ biological independent samples. **I** Kinetic of DNAM1 expression (left) and proliferation (right) of $TCR_{KO}TIGIT_{KO}$ and $TCR_{KO}TIGIT_{COMP}$ DKK1-specific (left) as in (**G**). $N = 3$ biological independent samples. **J** Working model for TIGIT deletion effects on low avidity tumor-specific T cells. Data are represented as mean ± s.e.m. Statistical analysis performed by paired two-tailed t-test unless otherwise stated. *, $P < 0.05$; **, $P < 0.01$. Source data and exact *p* values are provided as a Source Data file.

In summary, BE4max efficiently and safely generates $TCR_{KO}TIGIT_{KO}$ T cells thus representing an ideal tool for clinical translation.

TIGIT disruption converts low avidity T cells into potent anti-tumor effectors

In low-avidity MSLN-specific T cells, TIGIT knockout led to increased TCR signal strength, enhanced T cell avidity and improved degranulation. To test whether such improved functionality results in a superior anti-tumor activity, we exposed $TCR_{KO}TIGIT_{COMP}$ and $TCR_{KO}TIGIT_{KO}$ T cells, redirected with DKK1 or MSLN specific TCRs, to PDAC PDOs. Both DKK1-specific and MSLN-specific $TIGIT_{KO}$ T cells proved superior in killing PDAC PDOs in vitro, compared to their $TIGIT_{COMP}$ counterpart (Fig. 5A, B). To verify the effects of TIGIT knockout in a clinically relevant setting in vivo, we set up an orthotopic mouse model of human PDAC. Briefly, PDAC PDOs, transgenic for HLA-A*02:01$^+$ and expressing DKK1 and MSLN at similar levels (Supplementary Fig. 9A), were implanted into the pancreas of NSG mice, to recapitulate a primary lesion. Tumor-bearing mice were treated with a first loco-regional and a second systemic infusion of tumor-specific T cells (after 3 and 10 days from PDO injection, respectively, Fig. 5C). Consistently with their avidities, $TCR_{KO}TIGIT_{COMP}$ DKK1-specific T cells slowed down tumor growth (Fig. 5D), while no therapeutic effect was detected upon treatment with $TCR_{KO}TIGIT_{COMP}$ MSLN-specific T cells. Importantly, TIGIT disruption enabled MSLN-specific T cells to control tumor progression (Fig. 5E, F), with a consequent improvement of tumor bearing mice survival for up to 12 weeks (Fig. 5G, Supplementary Fig. 9B). On the other site, $TIGIT_{KO}$ had only a limited influence on DKK1-specific T cells, where it fastened tumor shrinkage (Fig. 5D). This difference in cytotoxicity cannot be explained by changes in persistence, differentiation, nor CD4/CD8 ratio of circulating cells, that were similar in $TCR_{KO}TIGIT_{COMP}$ and $TCR_{KO}TIGIT_{KO}$ T cells in both DKK1 and MSLN experimental groups (Supplementary Fig. 9C-I). We then analyzed circulating MSLN-specific T cells through high-dimensional flow cytometry for the expression of activation and/or exhaustion markers. Since no alterations were noticed in PD1, TIM3 and LAG3 kinetics (Supplementary Fig. 10A) upon TIGIT disruption, we mined data by cytoChain[62] to perform unbiased dimensionality reduction and clustering analysis, and confirmed that no differential enrichment of specific T cell subpopulations was detectable in $TCR_{KO}TIGIT_{COMP}$ and $TCR_{KO}TIGIT_{KO}$ MSLN-specific products (Supplementary Fig. 10B, C). Moreover, at 4 weeks from T cell injection, we observed an increased, although not significant, tumor infiltration by $TCR_{KO}TIGIT_{KO}$ MSLN-specific T cells compared to $TIGIT_{COMP}$ counterparts (Fig. 5H, I).

To verify whether the beneficial effect mediated by TIGIT knockout is maintained in a different gastrointestinal tumor setting, we challenged our MSLN-specific T cells with PDOs derived from CRC liver metastases. In vitro, $TCR_{KO}TIGIT_{COMP}$ MSLN-specific T cells failed to induce tumor killing while $TIGIT_{KO}$ counterparts efficiently eliminated CRC PDOs (Fig. 5J, S11A). We then tested our MSLN-specific cells in an orthotopic mouse model of CRC liver metastases[14]. Briefly, we injected CRC PDOs established from a liver metastasis into the liver of NSG mice to mimic the onset of liver lesions. After 3 days, mice were treated with a single intra-hepatic dose of tumor-specific T lymphocytes (Fig. 5K). Similarly to what we observed in PDAC, $TIGIT_{KO}$, but not $TIGIT_{COMP}$ MSLN-specific T cells mediated a potent therapeutic effect and promoted an overall disease-free survival of 100% (Fig. 5L). This striking anti-tumor activity was associated with a preferential, yet transient, expansion of $TCR_{KO}TIGIT_{KO}$ T cells (Supplementary Fig. 11B), with a phenotype and a CD4/CD8 ratio comparable to those of $TCR_{KO}TIGIT_{COMP}$ MSLN-specific T cells (Supplementary Fig. 11C, D).

All together, these data highlight a prominent role for TIGIT knockout in conferring low-avidity MSLN-specific engineered T cells the ability to shrink gastrointestinal tumors in vivo. This beneficial effect is linked to early T cell activation events, occurring upon T cell encounter with cancer cells. Our study provides an innovative and safe biotechnological strategy to fully exploit low-avidity TCRs and potentiate high-avidity ones, thus broadening the applicability of cellular therapy with TCR-engineered T cells for cancer treatment.

Discussion

Cell-based immunotherapies have transformed cancer treatment. Following the success of TILs therapy in melanoma[63], chimeric antigen receptors (CAR) T cells revolutionized the field of hematological malignancies[64], and recently the first TCR-based T cell therapy received FDA approval for synovial sarcoma[65,66]. However, solid tumors, accounting for 80% of new cancer diagnoses each year[5], present several challenges to ACT efficacy. Two major limitations are, the paucity of TCRs and CARs targeting relevant tumor antigens with proper strength, and the highly immunosuppressive TME. Thanks to the technological advances in genome editing, substantial efforts have been made to potentiate tumor recognition capacity and to overcome inhibitory/exhaustion mechanisms in engineered T cells[67–69].

TCRs targeting neoantigens are usually of high-affinity, but still patient-specific and not easily exploited by gene engineering approaches, while a large fraction of TCRs specific for TAAs display low affinity and low anti-tumor efficacy[2,3,44]. We hypothesized that genetic manipulation of T cells could increase the anti-tumor efficacy of low-avidity cells.

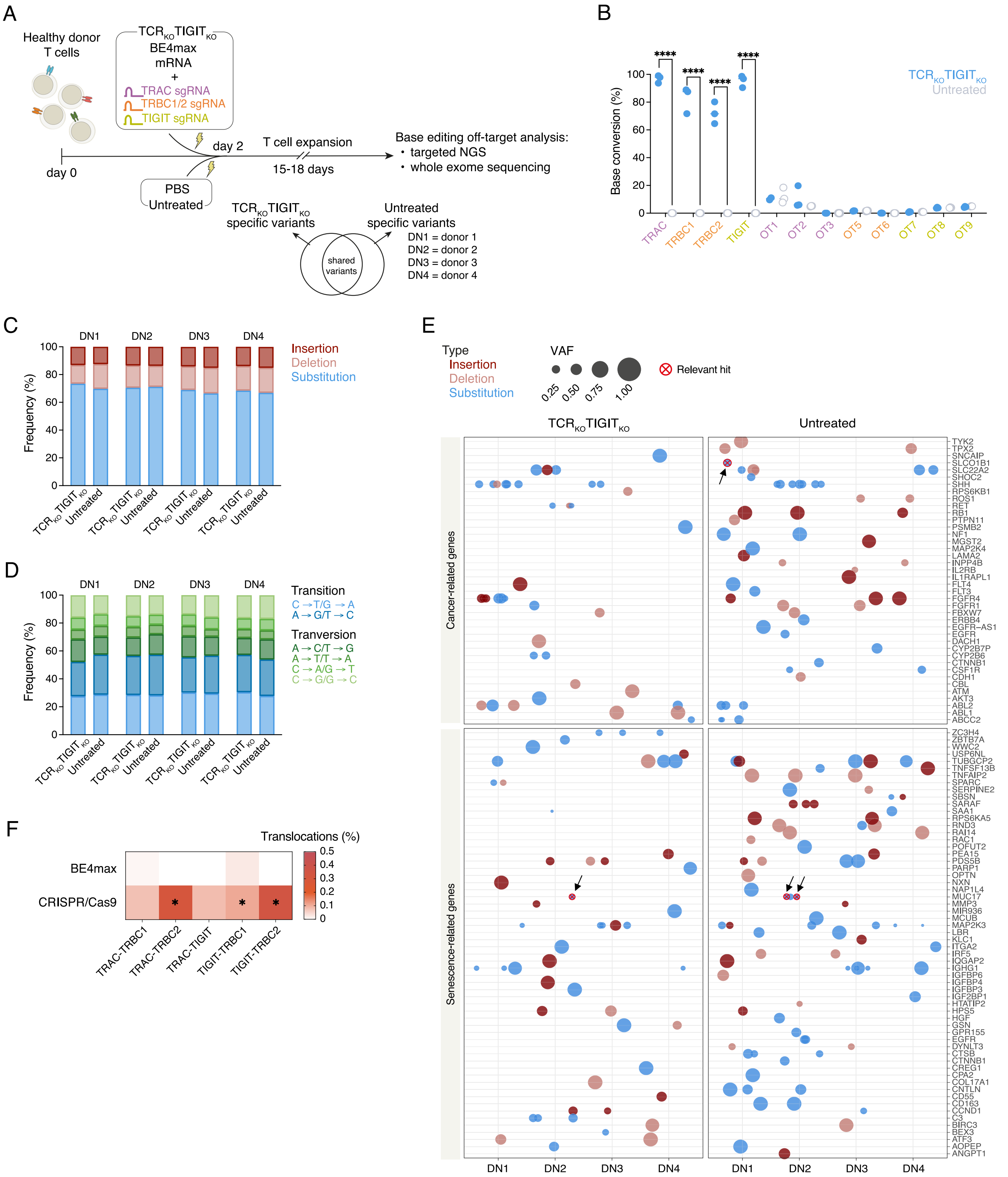

Fig. 4 | TCR$_{KO}$TIGIT$_{KO}$ T cells generated by BE4max display an optimal safety profile. A Schematics of the experiments shown in Figure 4 and Figure S6,7. **B** Frequency of nucleotide conversion quantified within the BE4max editing window (position 3-11 of sgRNAs) at on-target sites and predicted off-target loci (OT). Color code identifies OT for each sgRNA used. *N* = 3 biological independent samples. Statistical analysis by two-way ANOVA. The list of OT loci analyzed is shown in Supplementary Fig. 7A. Relative proportion of variants (**C**) and substitution types (**D**) in base edited TCR$_{KO}$TIGIT$_{KO}$ and mock electroporated (Untreated) T cells identified by WES and obtained after subtraction of germline variants. *N* = 4 matched biological independent samples. Statistical analysis by two-way ANOVA. **E** Bubble plot representing variants in cancer- and senescence- related genes obtained as in (**C**, **D**). Black arrows indicate missense mutations, classified as relevant hits. *N* = 4 matched biological independent samples. **F** Translocation frequencies between all target loci assessed by ddPCR in BE4max and CRISPR/Cas9 treated cells. Statistical analysis by paired two-tail t-test. *N* = 3 matched biological independent samples for each genome editing strategy. Data are represented as mean ± s.e.m. *, $P < 0.05$, ****, $P < 0.0001$. Source data and exact *p* values are provided as a Source Data file.

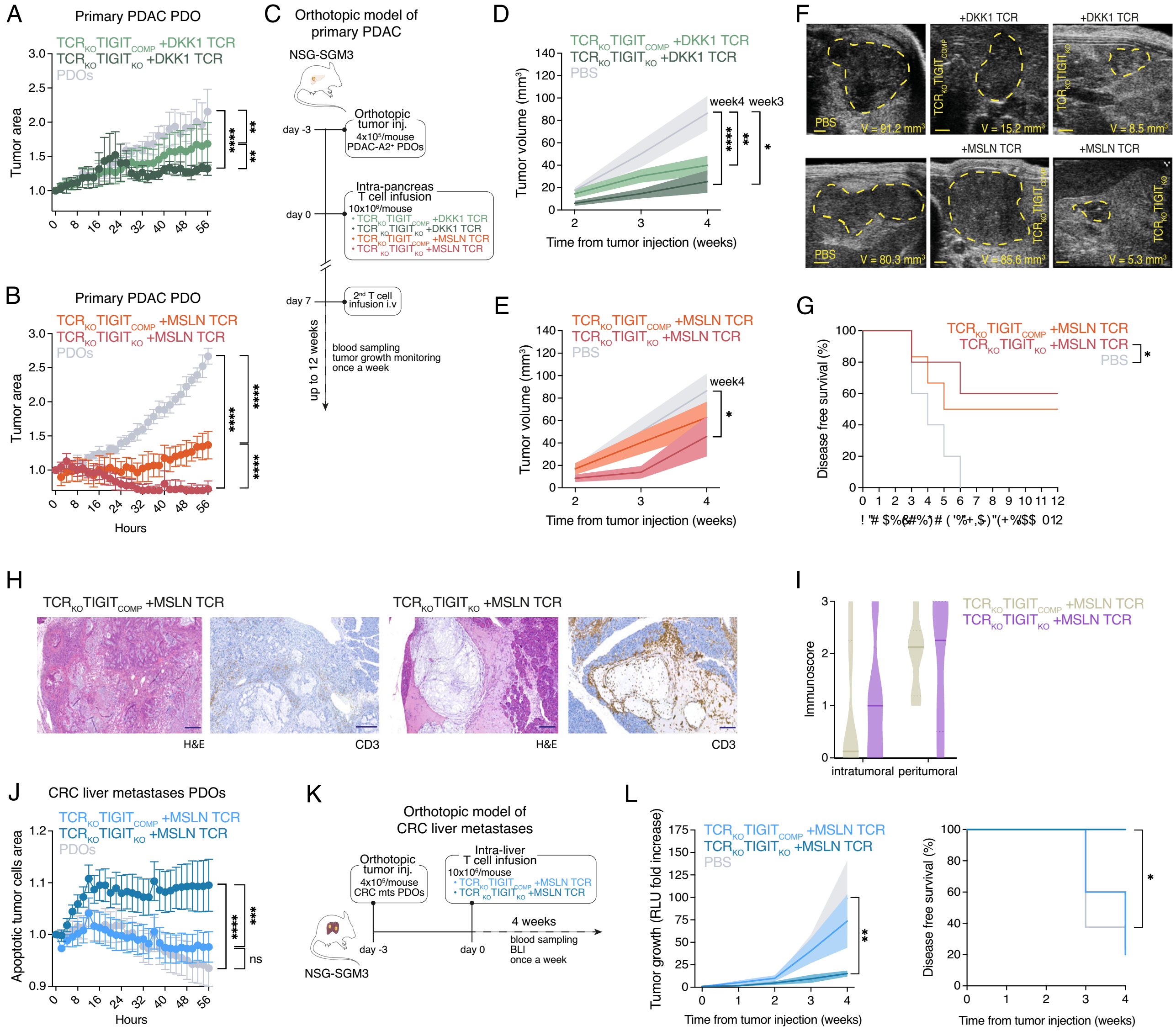

Fig. 5 | TIGIT disruption enables low-avidity T cells with potent anti-tumor activity. **A**, **B** Quantified IncuCyte cytotoxicity assays of a PDAC PDO treated with TCR$_{\mathrm{KO}}$TIGIT$_{\mathrm{KO}}$ or TCR$_{\mathrm{KO}}$TIGIT$_{\mathrm{COMP}}$ TAA-specific T cells at 10:1 effector-to-target ratio and monitored every two hours. Results from DKK1- and MSLN-specific T cells are displayed in A and B, respectively. $N = 3$ biological independent samples for each TCR; statistical analysis by linear regression. **C** Schematics of orthotopic xenograft PDAC mouse model used in the experiments in panel (**D**–**I**) and Supplementary Fig. 9,10. **D** Tumor progression measured by ultrasound imaging in PDAC bearing mice treated with TCR$_{\mathrm{KO}}$TIGIT$_{\mathrm{KO}}$ or TCR$_{\mathrm{KO}}$TIGIT$_{\mathrm{COMP}}$ DKK1-specific T cells. $N = 6$–11 mice per group ($N = 6$ TCR$_{\mathrm{KO}}$TIGIT$_{\mathrm{COMP}}$ group, $N = 6$ TCR$_{\mathrm{KO}}$TIGIT$_{\mathrm{KO}}$ group, $N = 11$ control group). Statistical analysis by two-way ANOVA. **E** Tumor progression measured by ultrasound imaging in PDAC bearing mice treated with TCR$_{\mathrm{KO}}$TIGIT$_{\mathrm{KO}}$ or TCR$_{\mathrm{KO}}$TIGIT$_{\mathrm{COMP}}$ MSLN-specific T cells. $N = 5$–11 mice per group ($N = 6$ TCR$_{\mathrm{KO}}$TIGIT$_{\mathrm{COMP}}$ group, $N = 5$ TCR$_{\mathrm{KO}}$TIGIT$_{\mathrm{KO}}$ group, $N = 11$ control group). Statistical analysis by two-way ANOVA. **F** Representative images of ultrasound measurement for 6 mice treated with PBS or engineered T cells. Scale bar 1 mm. **G** Kaplan-Meier survival curve of PDAC bearing mice treated with TCR$_{\mathrm{KO}}$TIGIT$_{\mathrm{COMP}}$ or with TCR$_{\mathrm{KO}}$TIGIT$_{\mathrm{KO}}$ MSLN-specific T cells and followed for 12 weeks. $N = 5$–6 mice per group ($N = 6$ TCR$_{\mathrm{KO}}$TIGIT$_{\mathrm{COMP}}$ group, $N = 5$ TCR$_{\mathrm{KO}}$TIGIT$_{\mathrm{KO}}$ group, $N = 5$ control group). Statistical analysis by Log-rank test. **H** Representative H&E and immunohistochemistry images of CD3^{+} T cells infiltrating PDAC of tumor bearing mice, as in E, treated with TCR$_{\mathrm{KO}}$TIGIT$_{\mathrm{COMP}}$ or TCR$_{\mathrm{KO}}$TIGIT$_{\mathrm{KO}}$ MSLN-specific T cells. Scale bar 100 µm. **I** Inflammation of PDAC-bearing mice at the tumor site upon treatment with MSLN-specific T cells as in (**E**). Inflammation was quantified based on a 0–3 score indicating the amount of human CD3^{+} T cells, and defined as immunoscore. $N = 6$ TCR$_{\mathrm{KO}}$TIGIT$_{\mathrm{COMP}}$ group, $N = 5$ TCR$_{\mathrm{KO}}$TIGIT$_{\mathrm{KO}}$ group. **J** Quantified IncuCyte cytotoxicity assay of PDOs from 2 CRC liver metastases treated with TCR$_{\mathrm{KO}}$TIGIT$_{\mathrm{KO}}$ or TCR$_{\mathrm{KO}}$TIGIT$_{\mathrm{COMP}}$ MSLN-specific T cells at 5:1 effector-to-target ratio and monitored every 2 h. Apoptotic PDOs area is calculated as the green+red area (PDOs stained in red, caspase 3/7 in green). $N = 3$ biological independent samples. Pooled data from $n = 2$ experiments. Statistical analysis by linear regression. **K** Schematics of orthotopic xenograft metastatic CRC mouse model used in the experiments in panel L and Supplementary Fig. 11. **L** Tumor progression measured by bioluminescent imaging of mice bearing CRC liver metastases and treated with TCR$_{\mathrm{KO}}$TIGIT$_{\mathrm{KO}}$ or TCR$_{\mathrm{KO}}$TIGIT$_{\mathrm{COMP}}$ MSLN-specific T cells (left). Disease-free survival (right) determined based on the average tumor growth rate of control mice. $N = 4$–8 mice per group ($N = 5$ TCR$_{\mathrm{KO}}$TIGIT$_{\mathrm{COMP}}$ group, $N = 4$ TCR$_{\mathrm{KO}}$TIGIT$_{\mathrm{KO}}$ group, $N = 8$ control group). Statistical analysis by two- way ANOVA and log-rank test, respectively. Data are represented as mean ± s.e.m. *, $P < 0.05$; **, $P < 0.01$; ***, $P < 0.001$; ****, $P < 0.0001$. Source data and exact p values are provided as a Source Data file. Mice images in C and K are provided by Servier Medical Art (https://smart.servier.com), licensed under a Creative Commons Attribution 3.0 Unported License.

To expand the current armamentarium against PDAC, and verify our hypothesis, we applied a funnel approach for the isolation and selection of TCR molecules endowing T cells with specific tumor killing capacity and a good safety profile. We employed our previously established TCR hunting pipeline[13,14] starting from the peripheral blood of healthy donors and cancer patients to expand rare tumor-reactive T cells. We isolated 5 distinct HLA-A*02:01 restricted TCRs and exploited them in a TCR-engineering framework. We investigated the avidity of each cellular product redirected with our TCRs, which is proportional to the TCR affinity, and the number of TCR molecules and coreceptors exposed on the cell surface[70]. In this way, we could classify our cells into high- (AGR2-, MUC5AC-, and DKK1-), and low- (MET and MSLN) avidity effectors and further focused on high-avidity DKK1- and low-avidity MSLN-specific products, which harbor high clinical value for their restricted expression in healthy tissues and overexpression in tumor cells.

We aimed at finding new biotechnological strategies to enhance the potency of low-avidity T cells and, to this purpose, we reasoned to disrupt TIGIT, an inhibitory molecule that clusters with the TCR at the immunological synapse following T cell activation, particularly abundant in T cells infiltrating PDAC[15].

Different mechanisms have been described in the attempt to elucidate how TIGIT controls T cell function. By ligand-dependent or -independent mechanisms, TIGIT can attenuate T cell co-stimulation by competing with CD226[17,45,52], also called DNAM1, and can suppress cytotoxic T-cell functions[17,45,56]. Comparing $\mathrm{TIGIT_{KO}}$ with $\mathrm{TIGIT_{COMP}}$ cells, we observed a similar downregulation of CD3 surface expression upon stimulation with peptide pulsed $\mathrm{CD155^{+}}$ target cells, indicating that TIGIT acts downstream to the TCR/CD3 complex. While TIGIT intracellular signaling partners have been well characterized in NK cells, their nature in T cells remains elusive[16]. Here, we specifically unveiled the impact of TIGIT disruption on TCR downstream signaling and linked it to functional activity of TCR-engineered T cells. The effect of TIGIT knockout in natural anti-tumor T cells, such as TILs, worth further investigation. We found that TIGIT gene disruption significantly enhances the TCR signal strength of low-avidity T cells only, by increasing the phosphorylation of ZAP70, which ultimately ameliorates their avidity and stabilizes the immunological synapses with cancer cells. Also, TIGIT disruption in NK cells ameliorates their cytotoxic capacity, by upregulating mTOR signaling and increasing their basal glycolytic rate[71]. However, in our context, we did not observe any effects of TIGIT knockout on the phosphorylation of S6, downstream molecule to mTORC1, nor glucose consumption. In T cells, TIGIT has been mainly described for its inhibition of DNAM1, a well-known adhesion molecule[52,53] which plays a major role in the immunological synapse formation and T costimulation when the antigen is presented by "non-professional" APCs, such as tumor cells[54,55,57]. We showed that DNAM1 surface expression levels decrease upon T cell activation in both low- and high-avidity T cells, with TIGIT disruption fostering a higher DNAM1 engagement in low-avidity MSLN-specific T cells only. Consistent with the observed increased proliferative capacity, TIGIT disruption completely rescued MSLN-specific T cells tumor killing ability in vitro and in vivo and mediated increased long-term mice survival, while conferring only modest functional benefit to high-avidity DKK1-specific T cells.

The clinical translation of therapeutic T cells manufactured through genome editing can be hindered by safety concerns. To address these, our TCR-edited T cell products have been designed to mitigate potential toxicity issues. TCRs were isolated from the circulating T cell memory pool of HLA-matched subjects[13,14], and none of them triggered autoimmune reactions in the respective donors. We selected TCRs that recognize antigens minimally expressed on healthy tissues, further reducing the risk of on-target, off-tumor toxicities. Additionally, we depleted the endogenous TCR α and β chains to prevent mispairing[11–14,31] and did not enhance TCR affinity, but focused on stabilizing T cell-cancer cell interactions through TIGIT knockout. To complement the safety profile of our T cell therapy strategy, we evaluated off-target events associated with the engineering platform.

Recently, among 12 cases (out of 8006 analyzed follow-up patients) of secondary malignancies after CAR-T immunotherapies, 2 of them have been associated to potentially pathogenic CAR insertions[72–74]. Although these frequencies are low and well counterbalanced by the exceptionally high rate of clinical responses observed with registered CAR- T cells, this finding underlines the need for a thorough and comprehensive evaluation of the safety profile of engineered cellular products. Compared to conventional programmable DNA nucleases, i.e ZFNs, TALENs and CRISPR/Cas9, base editors promote gene disruption by single nucleotide substitutions avoiding the introduction of DNA double strand breaks (DSBs)[75], that have been associated to different off-target events causing loss of cellular fitness and potential pathological consequences[31,35,76–79]. These observations paved the way for the first clinical trial investigating the efficacy of CAR-T cells generated by base editors[32], but no base edited TCR-T cell products were developed until now to our knowledge.

To validate the safety of our tool and protocol for genome engineering, we deeply evaluated the safety profile of $\mathrm{TCR_{KO}TIGIT_{KO}}$ T cells. Comparing BE4max to CRISPR/Cas9, we observed that *TRAC*, *TRBC1/2* and *TIGIT* were simultaneously edited with similar efficiencies by the 2 technological tools. However, while CRISPR/Cas9 treated cells presented a low although detectable rate of translocations among on-target sites, none were found in T cells edited by BE4max. Interestingly, we did not measure base editing at predicted sgRNA-dependent off-target sites by NGS, as already reported with a smaller number of edits[32,80,81]. Also, by ultra-deep whole exome sequencing we observed only 1 missense mutation with unknown significance in a senescence-related gene in base edited cells from only 1 donor. Despite we used the most sensitive sequencing technologies currently available, the highly polyclonal nature of our T cell populations makes the detection of global mutational events challenging. The observed absence of genomic mutations is further supported by the lack of an aberrant clonal expansion during culture. Spurious genome deamination has been previously associated with CBE activity, although evaluated using cell-free models[82,83] or HEK293T[84]. In a recent work, we characterized the safety profile of base editors in hematopoietic stem and progenitor cells and showed how intrinsic qualities of target sites, optimization of BE constructs, and culture conditions contribute to determining the genotoxic impact of base editing[34]. Of notice, the amount of CBE mRNA used for our T cell products, is 11 times and 5 times lower than that used in similar works[34,84]. The susceptibility of T cells to genome manipulation might, at least in part, explain the reduced genotoxic effect observed in our therapeutic cellular products, compared to other cellular targets. Moreover, the putative contaminants of our TCR-engineering strategy, which are T cells depleted in TIGIT but still expressing their endogenous TCR, did not show signs of increased auto- or allo-reactivity.

In summary, these results provide evidence of TIGIT role in directly modulating TCR signal strength in TCR-engineered T cells and its suitability as a target for T cell base editing, to potentiate low-avidity effectors while simultaneously conferring anti-tumor T cells the ability to escape from a key inhibitory axis in PDAC.

Methods

Cell lines and cell culture

$\mathrm{BxPC3\text{-}A2^{+}}$ human PDAC cell line, SW480 colorectal cancer cell line, IGROV1 ovarian cancer cell lines, $\mathrm{K562\text{-}A2^{+}}$ leukemic cell line, were cultured in RPMI 1640 (Lonza/Euroclone) supplemented with 10% fetal bovine serum (FBS, Carlo Erba), 1% penicillin-streptomycin (Lonza) and 2 mM glutamine (Lonza). $\mathrm{BxPC3\text{-}A2^{+}}$ and $\mathrm{K562\text{-}A2^{+}}$ were genetically engineered with a lentiviral vector encoding for HLA-A*0201 and a puromycin selection cassette. T2 lymphoblastoid cell line and

HEK293T cells were cultured in IMDM (Lonza/Euroclone) supplemented with 10% FBS, 1% penicillin-streptomycin and 2 mM glutamine.

T cells isolation from PBMCs

Peripheral blood mononuclear cells (PBMCs) were freshly isolated from the peripheral blood of healthy donors or PDAC patients, harvested upon informed consent at San Raffaele Hospital, by density gradient centrifugation using Ficoll-Hypaque (LymphoprepTM, Fresenius). Isolated PBMCs were washed 3 times to remove platelets and counted by trypan-blue exclusion. Cells were either used for tumor-specific T cell isolation or T cell manufacturing.

Antigen selection and peptides

We analyzed 15 published gene expression profiles of PDAC primary samples[85–99] and followed the procedure highlighted in Supplementary Fig. 1A. We obtained a final list of 19 TAAs (AGR2, ANXA2, CEACAM6, DKK1, ECT2, ENO1, EPCAM, HER2, MET, MSLN, MUC1, MUC4, MUC5AC, MUC16, SERPINB3, TMPRSS4, TOP2a, TSPAN1, TWIST1) and added mutant KRAS. We then selected published peptides deriving from these antigens[25–29,100–113]. Peptides were synthesized by Genscript Biotech (Netherlands) to specifications of validated sequence, sterility, and absence of endotoxin. Peptides were re-hydrated following manufacturer's instruction and mixed in equal amounts in all pools at a concentration of 1 μg/ml per peptide. 25 subpools, each one containing up to 6 peptides (10 μg/ml per peptide), were generated according to specific mapping matrix, with each peptide being included in only two intersecting subpools. The TCR hunting pipeline was applied as previously described[13,14].

Immortalized B cells

Immortalized B cells were generated as previously described[13] from healthy donors' and PDAC patients' peripheral blood, collected upon informed consent at San Raffaele hospital. Autologous B cells were sorted from healthy donor 7 (HD7) and the PDAC patient PBMCs by using the CD19 microbeads (Miltenyi Biotec). By spin infection, B cells were transduced with a lentiviral vector encoding for the BCL6/BCL2L1 transgenes and cultured on a γ-irradiated (100 Gy) mouse fibroblast cell line stably expressing CD40L (3T3-CD40L) in a 10:1 ratio. B cells were maintained in IMDM supplemented with 10% FBS, 1% penicillin-streptomycin, 2 mM glutamine, and 50 ng/mL of IL- 21 (Peprotech).

TCR repertoire sequencing

RNA samples of tumor associated antigen (TAA)-specific T cells were collected at each stimulation round to track the TCR repertoire overtime. RNA was extracted employing the Arcturus Pico Pure RNA extraction kit (Life Technology) and CDR3 regions amplified by a modified rapid amplification of cDNA ends (RACE) approach[114,115]. Samples were sequenced by using an Illumina MiSeq Sequencer and CDR3 clonotypes identified with the MiXCR software[115]. Based on the CDR3 selection, TRAC and TRBC alignments were analyzed by IMGT software to define the proper TCRαβ chain sequences. The sequences were codon optimized and synthetized by Twist Bioscience.

Analysis of RNAseq data

For antigen expression analysis on patient samples, dataset was obtained from public bulk RNA-seq of primary and metastatic PDAC patients[30]. For the analysis, we followed the procedure described in our previous work[14]. Briefly, after preprocessing steps, including filtering, quality trimming, and adapter removal, reads were aligned to the human genome (GRCh38/hg38) using STAR (version 2.5.3a) with default parameters. Only reads uniquely mapped to the genome were retained for downstream analyses. Gene-level expression counts were calculated using featureCounts (version 1.6.4), summarized across all exons annotated in GENCODE (version 37). Following TMM normalization with EdgeR, transcript per million (TPM) values were used as the expression unit. Gene expression values were categorized into quartiles based on their distribution: low (first quartile), medium (second and third quartiles), and high (fourth quartile). The expression of selected antigens was extracted from the dataset and binned into quartiles for analysis and representation.

Immunohistochemistry on human samples

FFPE tissue slides from PDAC primary tumors, PDAC liver metastases, and healthy tissue samples, were collected after written informed consent according to the San Raffaele Scientific Institutional Ethical Committee guidelines. Three micron sections were stained with anti-human AGR2 (rabbit monoclonal antibody clone SN74-01, Novusbio), anti-human DKK1 (rabbit monoclonal antibody clone SC06-86, Thermofisher), anti-human MET (rabbit monoclonal antibody, clone D1C2, Cell Signaling), anti-MSLN (VENTANA MSLN SP74, Roche diagnostic), anti-human MUC5AC (VENTANA MUC5AC MRQ, Roche diagnostic) according to manufacturer instruction. After testing 4 different anti-human DKK1 antibodies, we chose the one reported here, which has the better but not sufficient background/signal noise. Indeed, RNA scope is used for the enrollment of patients in clinical trial using DKK1 as target for cancer treatment (DisTinGuish)[116].

Genome editing of T cells

PBMCs were isolated form HDs, enriched for CD3$^+$ cells using anti-CD3/-CD28 magnetic beads (Dynabeads; Invitrogen) and seeded at a concentration of 2×10^6 cells/mL in RPMI 1640 supplemented with 10% FBS, 1% penicillin-streptomycin, 2 mM glutamine, 5 ng/mL IL-7, 5 ng/mL IL-15. Two days after stimulation T cells were washed 3 times with PBS and cell number determined by trypan-blue exclusion. For singleplex experiments, 1×10^6 T cells were electroporated with 1 μg of sgRNA (Synthego) and 1.5 μg of optimized BE4max or ABE8.20 m mRNA. BE4max and ABE8.20 m mRNAs were synthetized and purified as previously described[34]. For multiplex experiments, up to 1×10^6 T cells were electroporated with 1 μg of total sgRNAs (0.5 μg for each sgRNA to produce TCR$_{KO}$ cells, 0.33 μg for each sgRNA to produce TCR$_{KO}$TIGIT$_{KO}$ cells) together with 1.5 μg of BE4max. For CRISPR/Cas9 comparison experiments, 1×10^6 T cells were electroporated with ribonucleoprotein complexes formed by SpCas9 (Synthego) with each sgRNA in a 1:3 ratio. The 4D-nucleofector (Lonza, Basel, Switzerland) and P3 kit was used with 1×10^6 T cells per 25 μL strip, and up to 5×10^6 T cells per 100 μL. T cells were allowed to recover for 10 min at 37 °C following electroporation and then seeded in X- VIVO supplemented with 5% FBS, 1% penicillin-streptomycin, 2 mM glutamine, 5 ng/mL IL-7, 5 ng/mL IL-15 at a concentration of 2×10^6 cells/mL. The day after, edited T cells were transduced with a bidirectional lentiviral vector (MOI = 4–5) containing the tumor-specific TCR. Six days after T cell isolation, Dynabeads were magnetically removed, cells washed, and seeded at 0.5×10^6 cells/mL. For in vivo experiments, T cells were plated in G-REX plates (VWR) according to manufacturer's instruction.

Assessment of gene disruption efficiency

Genomic DNA was isolated (DNeasy blood and tissue Kit, Qiagen) 12 days after the editing procedure (15 days from T cell activation). By PCR the Cas9-targeted loci were amplified and submitted for Sanger sequencing. PCR amplicons of base edited cells were analyzed using the web app EditR[117]. In CRISPR/Cas9 comparison experiments, PCR amplicons were analyzed using Inference of CRISPR Editing (ICE) algorithm (Synthego).

Lentiviral vectors

Each TAAs-specific (AGR2-, DKK1-, MET-, MUC5AC-, MSLN-) TCR α and β chains were cloned in a bidirectional lentiviral vector (LV), to promote balanced TCR chain expression[11]. Under the minimal CMV promoter with antisense orientation we cloned the TCR α chain, while the TCR β chains were cloned under the human PhosphoGlycerate Kinase

(PGK) promoter with sense orientation[118]. A bidirectional lentiviral vector encoding human HLA-A*0201 was developed and used to stably express HLA-A*0201 in HLA-A*0201 negative patient derived organoids (PDOs) and cell lines. A puromycin resistance cassette was cloned under the minimal CMV promoter with antisense orientation while the HLA-A*0201 gene was placed under the PGK promoter with sense orientation. Sanger sequencing of cloned products was performed to validate the cloning procedure. A commercially available LV encoding for luciferase under the control of a constitutive promoter and a neomycin resistance cassette (Addgene # 21471) was used to stably express luciferase in PDOs. LVs were packaged by an integrase competent third-generation construct and pseudotyped by the Vescicular Stomatitis Virsus (VSV) envelope[119].

Immunophenotyping by flow cytometry

For surface staining, cells were incubated with the appropriate cocktail of antibodies in FACS buffer consisting of 1X PBS plus 1% FBS. Staining was performed at RT for 10 min.

For intracellular staining assays, cells were collected after 6 h of co-culture and stained for their vitality with Zombie viability kit (BioLegend) for 5 min followed by 10 min incubation at RT with surface antibodies (anti-human CD3, anti-human CD4, anti-human CD8). Cells were fixed and permeabilized with Fix/Perm buffer set (BioLegend). Intracellular staining was performed with antibodies specific for human cytokines (anti-human IFNγ, anti-human TNFα, anti-human IL-2).

For phospho-flow assays, T cells were stained with CellTrace^{TM} Far Red (Invitrogen) before coculture with target cells. Cells were then collected and stained for their vitality with Zombie Violet for 10 min. Cells were fixed and permeabilized with Fix/Perm buffer set, followed by a blocking step with 1X PBS with 3%BSA for 30 min at RT. Intracellular staining was performed with antibodies specific for phosphoproteins (phospho-ERK1/2, phospho-ZAP70 or phospho-S6) for 1 h at RT. After washing, cells were incubated with anti-rabbit or anti-mouse fluorescently-labeled secondary antibodies for 30 min at 4 °C.

The list of antibodies used and appropriate working concentration is reported in Supplementary Table 1. Flow cytometry data were acquired using 1 of the following instruments: BD FACS Canto II (BD Biosciences) and BD Symphony (cohort II). Data analysis was performed using FlowJo software (Tree star Inc).

Functional assays for T cell recognition of target cells

To evaluate cytokine production TAAs-specific or TCR-edited T cells were co-cultured with HLA-A*0201 target cells, pulsed for 16 h with peptide pools and subpools (assembled as described above), or with individual peptides and an unrelated one (final concentration 10 µg/mL). As positive control of T cell functionality, TCR-edited T cells were stimulated with 50 ng/ml phorbol myristate acetate (PMA, Sigma-Aldrich) and 1 µg/ml ionomycin (Sigma-Aldrich). The co-culture was plated in IMDM supplemented with 10% FBS, 1% penicillin- streptomycin, 2 mM glutamine plus 1 µg/ml anti-CD28 monoclonal antibody (BD Biosciences) and 1 µg/ml Golgi Stop protein transport inhibitor (BD Biosciences). Immediately after seeding we added anti-human CD107a antibody (7.5 µg/ml). Six hours later we stained the co-culture for intracellular cytokine detection.

To assess the ability of TCR-edited T cells to recognize naturally processed antigens and eliminate cancer cells, TCR-edited T cells were co- cultured with antigen positive HLA-A*0201 PDAC cell line (BxPC3-A2$^+$), antigen low/negative (SW480) and HLA unrelated controls (IGROV1) for 24 h at 5:1 effector-to-target ratio normalizing the amount of T cells based on the CD3 surface expression. Prior to co-culture, target cells were counted, seeded and stimulated overnight with 200 ng/mL human recombinant IFNγ (Peprotech). The co-culture was plated in IMDM supplemented with 10% FBS, 1% penicillin-streptomycin, 2 mM glutamine plus 1 µg/ml anti-CD28 monoclonal antibody. The number of residual target cells was determined by live/dead staining and flow cytometry to calculate the cytotoxicity: [(1-(number of residual target cells in the presence of TCR-edited T cells/number of residual target cells when seeded alone))*100].

T cell avidity assays

K562-A2$^+$ were plated at 1–1.5 × 10^6 cells/mL in RPMI supplemented with 10% FBS, 1% penicillin- streptomycin, 2 mM glutamine and pulsed overnight with individual peptides and an unrelated one (final concentration 10 µg/mL). The following day target cells were washed, resuspended at 80 × 10^6 cells/mL and attached on concanavalin A (Merck) according to Z-Movi instructions.

For T cell avidity comparison, T cells from 3 HDs were edited to deplete the endogenous TCR and transduced in separate wells with LVs encoding for each TAA- specific TCR. To normalize for TCR expression and co-receptor dependance, T cell were sorted for CD3 surface expression and cryopreserved until use. Upon thawing, T cells were sorted for CD8 and maintained in culture for 2 days before proceeding with the avidity assays. 1 × 10^6 TAAs-specific T cells were stained with CellTrace far-red (Thermofisher Scientific). Each TAA-specific T cell sample was run on the specific chip and an unrelated one. For $TIGIT_{COMP}$ and $TIGIT_{KO}$ comparison, $TCR_{KO}TIGIT_{COMP}$ and $TCR_{KO}TIGIT_{KO}$ T cells were transduced with DKK1- or MSLN-specific TCRs. Bulk T cell populations were stained with CellTrace far-red (Thermofisher Scientific). Each TAA-specific T cell sample was run on the specific chip and an unrelated one. T cells were incubated on the chip for 5 min before applying the acoustic force. Relative avidity was calculated by the percentage of cells bound to the specific peptide/percentage of cells bound to the unrelated peptide. To compare the avidity of different T cell products, non-linear regression models were fitted to each dataset to calculate the kneedle point (Arvai, K. (2023). kneed (v0.8.5). Zenodo. https://doi.org/10.5281/zenodo.8127224).

Glucose uptake assay

K562-A2$^+$ were pulsed overnight with a TCR-specific or an unrelated peptide (final concentration 10 µg/mL). TCR-edited $TIGIT_{COMP}$ or $TIGIT_{KO}$ T cells from 3 HDs were cocultured at a 1:1 ratio with peptide pulsed K562-A2$^+$ cells and collected at 24 and 48 h upon coculture. Cells were stained with 2-(N-(7-Nitrobenz-2-oxa-1,3-diazol-4-yl)Amino)-2-Deoxyglucose (2-NBDG, ThermoFisher Scientific) as previously described[120]. The uptake of 2-NBDG, as surrogate for glucose uptake, was evaluated by flow cytometry using a Canto II cytometer (BD Bioscience).

Organoids generation and maintenance

PDOs originated from CRC liver metastases were produced as previously described[14,121]. Briefly, freshly isolated samples were minced and incubated 2 times with 5 mL PBS/EDTA 5 mM at RT for 15'. Tumor tissues were enzymatically digested with a solution of TrypLE (Gibco) 2X in PBS/EDTA 1 mM for 30–60 min. Cancer cells released in the supernatant were collected and washed with Basal Medium composed of Advanced DMEM/F12 (Thermo Fisher) supplemented with 1% penicillin- streptomycin, 2 mM glutamine, 10 mM HEPES (Thermo Fisher) and 50ug/mL Primocin (Invivogen). Cell pellets were resuspended in Matrigel (Corning) and seeded in 24-well plates. CRC specific culture medium was added after Matrigel polymerization. PDAC PDOs were generated as previously described[122]. Briefly, PDAC tissues were minced and digested with 5 mg/mL collagenase II solution in Advanced DMEM/F12 for 2 h at 37 °C. Cells were washed, resuspended with Matrigel and plated in 24-wells. PDAC specific culture medium was added after Matrigel polymerization consisting in Basal Medium supplemented with 1X B27, 1X N2, 50 ng/mL recombinant EGF, 100 ng/mL recombinant Noggin, 250 ng/mL R-spondin 3 (PeproTech), 10 nM Gastrin, 100 ng/mL FGF-10, 100 ng/mL Wnt-3A, 10 uM Y27-632, 4 mM Nicotinamide, 2.5 mM N-acetyl cysteine, 0.5 uM A83-01. To split organoids, growth medium was removed and Matrigel domes were incubated with 500 uL of 1 U/mL Dispase II (Sigma-Aldrich) in Basal Medium at 37 °C for 1 h. Following Matrigel digestion, organoids were collected and washed with PBS at 1200 rpm for 5 min. To expand them cell pellets were resuspended in TrypLE 1X and incubated up to 15′ at 37 °C to obtain a single cell suspension. After that, organoids were washed 2 times with PBS and centrifuged 300 g for 5 min. Following the removal of supernatant, cell pellets were mixed with new Matrigel and plated as described above.

To generate PDO-luc organoids, PDOs were transduced with an LV encoding for luciferase under the control of a constitutive promoter and a neomycin resistance cassette (Addgene # 21471). Briefly, PDOs were digested with TrypLE 1X to obtain a single cell suspension and resuspended at a concentration of 0.5×10^6 cells/mL in Advanced DMEM/F12 containing the lentiviral vector and 8 µg/ml of Polybrene (Sigma-Aldrich). After spin infection, cells were allowed to recover for 2 h at 37 °C and then plated as usual. PDOs were maintained with antibiotic selection for at least 3 weeks and then checked for luciferase expression. PDOs with stable expression of HLA-A*0201 were generated by employing the same strategy.

Incucyte cytotoxicity assays of PDAC and CRC PDOs

To evaluate the killing of patient-derived organoids we used the Incucyte Live Imaging system. For PDAC PDOs killing, PDOs were counted, embedded into Matrigel droplets, and plated overnight at a concentration of 1×10^5/well in Basal medium supplemented with 200 ng/mL human recombinant IFNγ. The following day, PDOs were released from the Matrigel and mixed with T cells at 10:1 effector-to-target ratio in 50 µL of 50% Matrigel solution (50% Matrigel-50% Basal medium). Upon Matrigel polymerization, basal medium supplemented with 1 µg/ml anti-CD28 monoclonal antibody was added. Images were collected every 2 h and organoids area was quantified. For CRC PDOs killing, PDOs were released from the Matrigel and plated overnight at a concentration of $30–50 \times 10^4$/mL in Basal medium supplemented with 200 ng/mL human recombinant IFNγ[123]. The following day, PDOs were labeled with 1 µM Cytolight Rapid Red Dye (Sartorius) following manufacturer's instruction. Cells were seeded at 5:1 effector-to-target ratio in IMDM supplemented with 10% FBS, 1% penicillin-streptomycin, 2 mM glutamine plus 1 µg/ml anti-CD28 monoclonal antibody and 5 µM of Caspase-3/7 Green (Sartorius). Images were collected every 2 h and apoptotic cell area was quantified by measuring the green signal in red PDOs.

In vivo experiments

All mice experiments received ethical approval by the Institutional Animal Care and Use Committee. Mice were maintained in Specific Pathogen-free (SPF) animal research facilities with a 12 h/12 h dark/light cycle and standardized temperature (22 ± 2 °C) and humidity (55 ± 5%).

For the in vivo assessment of anti-tumor efficacy in PDAC setting, we employed 7–10-week-old male non-irradiated immunodeficient NSG (NSG-SGM3) mice from Jackson Labs. Each mouse was intra-pancreatic injected with 4×10^4 Antigen$^+$ PDAC PDOs transgenic for the HLA-A*0201. Two sequential doses of TCR-edited TIGIT$_{COMP}$ or TCR-edited TIGIT$_{KO}$ T cells (10×10^6 CD3$^+$ cells) were delivered first by an intra-pancreatic injection and second by i.v injection, 3 and 10 days from tumor infusion respectively. Tumor control was evaluated measuring tumor volume by ultrasound imaging performed using a high-performance ultrasonographic scanner designed for small animal imaging (Vevo 2100 FUJIFILM VisualSonics, Inc., Toronto, ON, Canada). For surgical and analytical procedures, mice were anaesthetized (flurane; Isoba, Schering-Plough, USA, 4% in oxygen for induction, 2% for maintenance at a rate of 1 L/minute. 2D and 3D Ultrasound images in B-mode were taken using the linear probe MicroScan MS 550D (22–55 MHz; fc 40 MHz; FUJIFILM VisualSonics, Inc., Toronto, ON, Canada). To obtain the tumors' 3D images, the scanner was mounted on the Vevo Imaging Station (part of the VisualSonics Vevo Integrated Rail System III) equipped with a 3D motor stage and positioned on the tumor region. The 3D images were built by acquiring 2D images every 140 µm over the whole length of the tumor. Images were analyzed off-line using the Vevo LAB analysis software (Fujifilm VisualSonics Inc., Toronto, ON, Canada) by a dedicated operator.

For the in vivo assessment of anti-tumor efficacy in mCRC setting, we employed 7-10-week-old male non-irradiated immunodeficient NSG (NSG-SGM3) mice from Jackson Labs. Each mouse was intra-hepatically injected with 4×10^4 LUC+ mPDOs (HLA-A0201 positive, antigen positive)[14]. After three days, a single dose of TCR-edited TIGIT$_{COMP}$ or TCR-edited TIGIT$_{KO}$ T cells were delivered by intra-hepatic injection (10×10^6 CD3+ cells). Tumor control was evaluated using small animal bioluminescence imaging (BLI) with the In Vivo Imaging System (IVIS® SpectrumCT, PerkinElmer, USA). Each mouse received an intraperitoneal injection of D-luciferin (PerkinElmer) 150 mg/kg body weight 10 min before BLI. Mice were kept at RT and anaesthetized as before for image acquisition. Images were analysed using Living Image 4.5 (Perkin Elmer, Waltham, MA, USA) by measuring the total flux (photons/s) within the selected region of interest. Mice were euthanized when tumor burden reached 1×10^9 BLI, according to ethical committee guidelines.

To monitor T cell expansion overtime bleedings were performed once a week and T cells analyzed by flow cytometry.

Immunohistochemistry on murine pancreas sections

For immunohistochemical analysis on PDAC PDOs, 40×10^4 cells were injected into the pancreas of NSG mice. After euthanasia, organs were sampled, fixed in zinc-formalin and embedded in paraffin. 7 µm paraffin sections were stained with hematoxylin and eosin or further processed for immunohistochemical analyses using anti-human DKK1 (rabbit monoclonal antibody #SC06-86, Novusbio), anti-human MSLN (VENTANA MSLN SP74, Roche diagnostic), and anti-human CD66/CEA (rabbit monoclonal antibody, clone C66/2055 R, NSJ Bioreagents) following manufacturer's instruction. Immunohistochemical analysis was performed in automated BOND RX Leica Biosystem and images acquired using the Aperio Scanscope system (Leica Biosystems).

Quantification of immune synapses by Imaging Flow Cytometry

For analysis of immune synapses, dissociated mCRC PDOs cells were stained with 0.6 µM Cytolight Rapid Red Dye according to manufacturer's instruction. Stained PDOs were cocultured with T cells at 5:1 effector-to-target ratio. After 45 min, cells were fixed using the fixation buffer of the Fix/Perm buffer set (BioLegend) and then stained with anti-human CD3 in Pacific Blue to identify T cells. Cells were then washed, permeabilized (Fix/Perm buffer set) and stained with Phalloidin-FITC for F-actin.

Acquisition of images was performed with ImagestreamX Mark II System (Amnis, Cytek Biosciences). Following acquisition, data were analyzed by IDEAS 6.2 software. Couplets made of one T cell and one PDO cell where used for the identification of synapses thorugh an Interface mask was generated. To generate the interface mask, a Morphology function on Ch01 (CD3-Pacific Blue staining) was used to create the Cell of Interest (T cells) mask, and a mask on the brightfield channel that covers both objects involved in the synapses was selected as Conjugate Mask. For the latter, a component function (area as ranking feature, descending order with a rank of 1) was applied on the object function mask in brightfield channel to better identify only doublets that were in close contact. The Interface mask was then used to identify the T-PDO synapse site and to better cover the cell contact region a dilation of 6 pixels was used. To identify real synapses, we looked at the increase of F-actin at the cell contact region, where F-actin polimerize and concentrate[51]. For this purpose, the total amount of F-actin was measured both in T cells (Intensity_Morphology

(M01,Ch01)_Ch02) and at the synapse site (Intensity_Interface mask_Ch02), and the % of enrichment was measured as follows:

F actin enrichment (%) = (Intensity_Interface mask_Ch02 / Intensity_Morphology (M01,Ch01)_Ch02)* 100.

Only doublets with F-actin enrichment >30% in the immune synapse were considered and among them a further selection was done taking advantage of Bright Detail Similarity_Interface mask_Ch01_Ch05, through which the colocalization of CD3 and Cytolight within the immunological synapse can be evaluated, versus Bright Detail Intensity_interface mask_Ch02 that computes high local pixel intensity of Phalloidin staining at the synapse site.

Droplet digital PCR (ddPCR) for translocation quantification and vector copy number

Translocation assays were designed with two primers, amplifying the translocation product, plus one probe designed to bind near the cut site. Three independent donors of untreated, base edited and CRISPR/Cas9 edited cells were run as a duplexed assay formed by an experimental primer+probe combination (FAM) specific for a translocation outcome (BioRad) and the internal reference prime+probe combination (VIC) amplifying the human GAPDH (Thermofisher Scientific). Reactions were made with 50 ng of genomic DNA per each assay and the ddPCR Supermix for Probes (no dUTP) (BioRad) following the manufacturer's instructions. Droplets were generated and analyzed using QX200 Droplet-digital PCR system (BioRad). Frequency was calculated as fractional abundance adjusted for two-copies of reference sequence per genome using the QuantaSoft ver 14.0 software (BioRad). Integrated LV copies were quantified a duplexed assay by amplifying the LV vector with a custom assay and the internal reference prime+probe combination (VIC) amplifying the human GAPDH (Thermofisher Scientific).

sgRNA-dependent off target analysis

Off-target sites for each sgRNA were predicted using the web app CRISPOR and filtered to be located into exons. Top off-target sites were selected (8 total) and genomic DNA extracted 14 days after the editing procedure (DNeasy blood and tissue Kit, Qiagen). Primers (NGS grade, Eurofins) were designed to amplify a 300–500 bp region centered on the off-target sequence. Genomic DNA was amplified using PlatinumTMSuperFiTM DNA polymerase (Thermofisher Scientific), high fidelity according to the manufacturer's protocol, using the cycle [98 °C-30"]-[98 °C-5']- 24x[gradient 65°-55 °C-30", 72 °C-30"]-[72 °C-5']-[4 °C-hold]. For OT8 the number of cycles was increased to 35. Amplicons were purified from 2% agarose gel (QIAquick Gel Extraction Kit, Qiagen) and submitted to Eurofins for amplification with indexing adaptors and sequencing on an Illumina MiSeq 2x300bp run. Sequencing data were analysed with CRISPResso2 (Clement 2019) to detect and quantify of insertions, mutations and deletions. First, input NGS sequences were trimmed using the Trimmomatic software (http://www.usadellab.org/cms/?page=trimmomatic) based on the phred33 score to remove low-quality positions (score <30) and Illumina adapters, keeping only trimmed reads having length greater than 100 bp to ensure a good coverage of the reference region (CRISPResso2 options: --trim_sequences --trimmomatic_command trimmomatic --trimmomatic_options_string 'ILLUMINACLIP:TruSeq3-PE-2.fa:2:30:10 MINLEN:100'). The cleaned sequences were mapped to the corresponding input reference locus region (i.e., on/off-target depending on the sample) and RNA guides were provided to focus the analysis on that specific region. Specifically, the computed alleles were quantified within the sgRNA sequences (that represent the editing window of the base editor) by measuring the number of reads and their relative abundances based on total read counts. Moreover, both the targeted and the produced nucleotide were provided (CRISPResso2 options: --base_editor_output --conversion_nuc_from C/G --conversion_nuc_to T/A), to measure the frequency of substitutions. Finally, CRISPResso2 output alleles were post-processed by correcting all the mismatch positions outside the quantification window and re-quantifying the total read counts (and consequently the corresponding relative abundances). Alleles showing a relative abundance lower than the false positive threshold (set at 0.2% based on untreated samples) were filtered out. Comparing untreated to base edited samples, the results were obtained by classifying and quantifying the (expected) SNVs of the base editor, other SNVs, insertions, and deletions, as well as their combinations. Together with the off-target loci, we sequenced T cells in TRAC, TRBC1, TRBC2 and TIGIT as positive controls of editing efficiency.

sgRNA-independent off-target analysis

Base edited cells disrupted in TRAC, TRBC1, TRBC2, and TIGIT, and electroporated cells, as untreated controls, were generated from 4 healthy donors. Genomic DNA was isolated in sterile conditions (DNeasy blood and tissue Kit, Qiagen) at the end of the manipulation procedure (17 days of in vitro culture). Whole Exome Sequencing was performed by Genewiz (Azenta) using the Agilent SureSelect Human All Exon V7 kit and running an Illumina NovaSeq 2x150bp with an estimated coverage of 500X per sample, and input data were analyzed following the GATK "Best Practice Workflows" to identify variants in each sample. In details, FastQC (v0.11.9) was used to check the quality of the sequencing reads, trim-galore (v0.6.6) was employed to trim low-quality bases, and then the Seqtk toolkit (v1.3) was used to randomly down- sample abundant samples to 190 M reads to avoid sample unbalance. After that, input sequences were aligned to the human genome assembly (GRCh38) using BWA (v0.7.17). The computed alignments were processed with Picard (v2.25.6) MarkDuplicates to mark duplicates and GATK (v4.2.0) BaseRecalibrator + ApplyBQSR to recalibrate base quality scores on dbSNP known sites. HaplotypeCaller was used to call variants in each sample by emitting condensed non-variant blocks (i.e., -ERC GVCF), while CombineGVCFs and GenotypeGVCFs were employed to combine and genotype variants, respectively. VariantFiltration was then applied to filter results based on their 'QualityByDepth' (i.e., --filter-expression 'QD < 2.0') and overall coverage 'DP' (i.e., --filter-expression 'DP < 500'). Moreover, additional per-sample filters were applied on variants belonging to each sample to identify the private ones, that is, variants having low genotype quality (i.e., GQ < 80) and low coverage (i.e., DP < 50) were removed. The untreated sample of each donor was used as germline reference, and its variants were filtered out from the corresponding treated sample, as such variants were considered as already present in the initial cell population and not induced by the base editor. A final step was performed to get rid of multi-allelic variants (mainly involving repetitive sequences). SnpEff (v5.0) was used to annotate the resulting variants on the canonical isoform from the GRCh38.p13.RefSeq reference database, and the downstream analyses involved their classification according to the type (insertion, deletion, or SNV), with a specific focus on all SNVs to classify the specific mutation events. Assessment of variants on a panel of cancer related genes and on T cell related gene lists was performed based on variant annotations.

Evaluation of alloreactivity and autoreactivity

To assess the influence of TIGIT knockout on T cells still expressing their endogenous TCR after base editing, we enriched the culture for CD3+ cells by CD3 microbeads (MiltenyiBiotec). Reached their resting phase, T cells were stimulated twice with g-irradiated (30gy) PBMCs derived from 3 mismatched donors at 1:100 ratio. 7-10 days after the last stimulation, T cells were cocultured at 1:1 ratio with the same mismatched PBMCs or autologous PBMCs, and evaluated for their killing capacity and cytokine production as described earlier.

Statistical analyses

Sample size and statistical tests are described in the figures. Data are expressed as mean ± SEM unless otherwise specified. Statistical tests were performed using and Prism V.9.3.1 (GraphPad Software, San Diego, California, USA) and R statistical software (version 4.1.2; https://cran.r-project.org/index.html). *P* value adjusted tests were employed to identify significant differences between groups with more than three comparsions. *P* value < 0.05 was taken to indicate statistical significance.

Ethics statement

Healthy donors' samples were obtained upon written informed consent, according to the San Raffaele Scientific Institutional Ethical Committee guidelines. Patients' samples were collected at San Raffaele Hospital upon written informed consent, after San Raffaele Institutional Ethical Committee approval (NCT04622423). All pre-clinical in vivo experiments and procedures on mouse models were performed according to protocols approved by the Institutional Animal Care and Use Committee (IACUC) at San Raffaele Hospital animal facilities (IACUC numbers: 929 and 1478) and authorized by the Italian Ministry of Health and local authorities according to the Italian law.

Reporting summary

Further information on research design is available in the Nature Portfolio Reporting Summary linked to this article.

Data availability

The bulk PDAC RNA-seq data used in this study are available in Gene Expression Omnibus (GEO) database with accession number GSE151580. The publicly available healthy donor RNA-seq data used in this study are available in the GTEx database accessible at https://gtexportal.org/home/. Next-generation sequencing data are deposited at European Nucleotide Archive with the following accession numbers: PRJEB79006 (NHEJ) and PRJEB78986 (WES). Sequences for sgRNAs and primers to amplify edited sites, off-target loci and translocation products, are not provided and subject to patent application WO2025/003481. These sequences can be shared from the corresponding author upon request. The remaining data are available within the Article, Supplementary Information or Source Data file and/or from the corresponding author upon request. Source data file is provided with this paper.

Code availability

The scripts for all bioinformatic analyses of NHEJ and WES are freely available at http://www.bioinfotiget.it/gitlab/custom/bonini_tigit2024.

References

1. Uslu, U. & June, C. H. Beyond the blood: Expanding CAR T cell therapy to solid tumors. *Nat. Biotechnol.* 1–10 https://doi.org/10.1038/s41587-024-02446-2 (2024).
2. Purcarea, A. et al. Signatures of recent activation identify a circulating T cell compartment containing tumor-specific antigen receptors with high avidity. *Sci. Immunol.* **7**, eabm2077 (2022).
3. Schmidt, J. et al. Neoantigen-specific CD8 T cells with high structural avidity preferentially reside in and eliminate tumors. *Nat. Commun.* **14**, 3188 (2023).
4. Halbrook, C. J., Lyssiotis, C. A., Pasca di Magliano, M. & Maitra, A. Pancreatic cancer: Advances and challenges. *Cell* **186**, 1729–1754 (2023).
5. Siegel, R. L., Kratzer, T. B., Giaquinto, A. N., Sung, H. & Jemal, A. Cancer statistics, 2025. *Cancer J. Clin.* **75**, 10–45 (2025).
6. Kabacaoglu, D., Ciecielski, K. J., Ruess, D. A. & Algül, H. Immune checkpoint inhibition for pancreatic ductal adenocarcinoma: Current limitations and future options. *Front. Immunol.* **9**, 1878 (2018).
7. Rojas, L. A. et al. Personalized RNA neoantigen vaccines stimulate T cells in pancreatic cancer. *Nature* **618**, 144–150 (2023).
8. Sethna, Z. et al. RNA neoantigen vaccines prime long-lived CD8+ T cells in pancreatic cancer. *Nature* https://doi.org/10.1038/s41586-024-08508-4 (2025).
9. Steele, N. G. et al. Multimodal mapping of the tumor and peripheral blood immune landscape in human pancreatic cancer. *Nat. Cancer* **1**, 1097–1112 (2020).
10. Sivakumar, S. et al. Distinct immune cell infiltration patterns in pancreatic ductal adenocarcinoma (PDAC) exhibit divergent immune cell selection and immunosuppressive mechanisms. *Nat. Commun.* **16**, 1397 (2025).
11. Provasi, E. et al. Editing T cell specificity towards leukemia by zinc finger nucleases and lentiviral gene transfer. *Nat. Med.* **18**, 807–815 (2012).
12. Mastaglio, S. et al. NY-ESO-1 TCR single edited stem and central memory T cells to treat multiple myeloma without graft-versus-host disease. *Blood* **130**, 606–618 (2017).
13. Ruggiero, E. et al. CRISPR-based gene disruption and integration of high-avidity, WT1-specific T cell receptors improve antitumor T cell function. *Sci. Transl. Med.* **14**, eabg8027 (2022).
14. Potenza, A. et al. Revealing and harnessing CD39 for the treatment of colorectal cancer and liver metastases by engineered T cells. *Gut* **72**, 1887–1903 (2023).
15. Worboys, J. D. et al. TIGIT can inhibit T cell activation via ligation-induced nanoclusters, independent of CD226 co-stimulation. *Nat. Commun.* **14**, 5016 (2023).
16. Manieri, N. A., Chiang, E. Y. & Grogan, J. L. TIGIT: A key inhibitor of the cancer immunity cycle. *Trends Immunol.* **38**, 20–28 (2017).
17. Johnston, R. J. et al. The immunoreceptor TIGIT regulates antitumor and antiviral CD8(+) T cell effector function. *Cancer Cell* **26**, 923–937 (2014).
18. Cui Zhou, D. et al. Spatially restricted drivers and transitional cell populations cooperate with the microenvironment in untreated and chemo-resistant pancreatic cancer. *Nat. Genet* **54**, 1390–1405 (2022).
19. Freed-Pastor, W. A. et al. The CD155/TIGIT axis promotes and maintains immune evasion in neoantigen-expressing pancreatic cancer. *Cancer Cell* **39**, 1342–1360.e14 (2021).
20. Yousuf, S. et al. Spatially resolved multi-omics single-cell analyses inform mechanisms of immune dysfunction in pancreatic cancer. *Gastroenterology* **165**, 891–908.e14 (2023).
21. Heiduk, M. et al. TIGIT expression delineates T-cell populations with distinct functional and prognostic impact in pancreatic cancer. *Clin. Cancer Res. J. Am. Assoc. Cancer Res.* **29**, 2638–2650 (2023).
22. Werba, G. et al. Single-cell RNA sequencing reveals the effects of chemotherapy on human pancreatic adenocarcinoma and its tumor microenvironment. *Nat. Commun.* **14**, 797 (2023).
23. Rousseau, A., Parisi, C. & Barlesi, F. Anti-TIGIT therapies for solid tumors: A systematic review. *ESMO Open* **8**, 101184 (2023).
24. Sundstrom, E. C., Huang, X. & Wiemer, A. J. Anti-TIGIT therapies: A review of preclinical and clinical efficacy and mechanisms. *Cancer Immunol. Immunother. CII* **74**, 272 (2025).
25. Lee, H. J. et al. Identification of novel HLA-A*0201-restricted epitopes from anterior gradient-2 as a tumor-associated antigen against colorectal cancer. *Cell. Mol. Immunol.* **9**, 175–183 (2012).
26. Qian, J. et al. Dickkopf-1 (DKK1) is a widely expressed and potent tumor-associated antigen in multiple myeloma. *Blood* **110**, 1587–1594 (2007).
27. Schag, K. et al. Identification of C-met oncogene as a broadly expressed tumor-associated antigen recognized by cytotoxic T-lymphocytes. *Clin Cancer Res.* **10**, 3658–3666 (2004).
28. Tsukagoshi, M. et al. Identification of a novel HLA-A24-restricted cytotoxic T lymphocyte epitope peptide derived from mesothelin in pancreatic cancer. *Oncotarget* **9**, 31448–31458 (2018).

29. Yamazoe, S. et al. Identification of HLA-A*0201- and A*2402-restricted epitopes of mucin 5AC expressed in advanced pancreatic cancer. *Pancreas* **40**, 896–904 (2011).
30. Yang, J. et al. Integrated genomic and transcriptomic analysis reveals unique characteristics of hepatic metastases and pro-metastatic role of complement C1q in pancreatic ductal adenocarcinoma. *Genome Biol.* **22**, 4 (2021).
31. Stadtmauer, E. A. et al. CRISPR-engineered T cells in patients with refractory cancer. *Science* **367**, eaba7365 (2020).
32. Chiesa, R. et al. Base-Edited CAR7 T cells for relapsed T-cell acute lymphoblastic leukemia. *N. Engl. J. Med.* **389**, 899–910 (2023).
33. Cianciotti, B. C. et al. TIM-3, LAG-3, or 2B4 gene disruptions increase the anti-tumor response of engineered T cells. *Front. Immunol.* **15**, 1315283 (2024).
34. Fiumara, M. et al. Genotoxic effects of base and prime editing in human hematopoietic stem cells. *Nat. Biotechnol.* **42**, 877–891 (2024).
35. Webber, B. R. et al. Highly efficient multiplex human T cell engineering without double-strand breaks using Cas9 base editors. *Nat. Commun.* **10**, 5222 (2019).
36. Larson, R. C. et al. CAR T cell killing requires the IFNγR pathway in solid but not liquid tumours. *Nature* **604**, 563–570 (2022).
37. Leick, M. B. et al. Non-cleavable hinge enhances avidity and expansion of CAR-T cells for acute myeloid leukemia. *Cancer Cell* **40**, 494–508.e5 (2022).
38. Oliveira, G. & Wu, C. J. Dynamics and specificities of T cells in cancer immunotherapy. *Nat. Rev. Cancer* **23**, 295–316 (2023).
39. Carr, A. et al. Advances in preclinical TCR characterization: leveraging cell avidity to identify functional TCRs. *Biol. Chem.* **405**, 517–529 (2024).
40. Majzner, R. G. & Mackall, C. L. Tumor antigen escape from CAR T-cell therapy. *Cancer Discov.* **8**, 1219–1226 (2018).
41. Gardner, R. et al. Acquisition of a CD19-negative myeloid phenotype allows immune escape of MLL-rearranged B-ALL from CD19 CAR-T-cell therapy. *Blood* **127**, 2406–2410 (2016).
42. Da Vià, M. C. et al. Homozygous BCMA gene deletion in response to anti-BCMA CAR T cells in a patient with multiple myeloma. *Nat. Med.* **27**, 616–619 (2021).
43. Choi, B. D. et al. Intraventricular CARv3-TEAM-E T cells in recurrent glioblastoma. *N. Engl. J. Med.* **390**, 1290–1298 (2024).
44. Oliveira, G. et al. Phenotype, specificity and avidity of antitumour CD8+ T cells in melanoma. *Nature* **596**, 119–125 (2021).
45. Banta, K. L. et al. Mechanistic convergence of the TIGIT and PD-1 inhibitory pathways necessitates co-blockade to optimize anti-tumor CD8+ T cell responses. *Immunity* **55**, 512–526.e9 (2022).
46. van Leeuwen, J. E. & Samelson, L. E. T cell antigen-receptor signal transduction. *Curr. Opin. Immunol.* **11**, 242–248 (1999).
47. Michel, F., Attal-Bonnefoy, G., Mangino, G., Mise-Omata, S. & Acuto, O. CD28 as a molecular amplifier extending TCR ligation and signaling capabilities. *Immunity* **15**, 935–945 (2001).
48. Shah, K., Al-Haidari, A., Sun, J. & Kazi, J. U. T cell receptor (TCR) signaling in health and disease. *Signal Transduct. Target. Ther.* **6**, 1–26 (2021).
49. Bunnell, S. C., Kapoor, V., Trible, R. P., Zhang, W. & Samelson, L. E. Dynamic actin polymerization drives T cell receptor-induced spreading: a role for the signal transduction adaptor LAT. *Immunity* **14**, 315–329 (2001).
50. Su, X. et al. Phase separation of signaling molecules promotes T cell receptor signal transduction. *Science* **352**, 595–599 (2016).
51. Wabnitz, G., Kirchgessner, H. & Samstag, Y. Qualitative and quantitative analysis of the immune synapse in the human system using imaging flow cytometry. *J. Vis. Exp. JoVE* https://doi.org/10.3791/55345 (2019).
52. Shibuya, A. et al. DNAM-1, a novel adhesion molecule involved in the cytolytic function of T lymphocytes. *Immunity* **4**, 573–581 (1996).
53. Shibuya, K. et al. Physical and functional association of LFA-1 with DNAM-1 adhesion molecule. *Immunity* **11**, 615–623 (1999).
54. Shibuya, K. et al. CD226 (DNAM-1) is involved in lymphocyte function-associated antigen 1 costimulatory signal for naive T cell differentiation and proliferation. *J. Exp. Med.* **198**, 1829–1839 (2003).
55. Gilfillan, S. et al. DNAM-1 promotes activation of cytotoxic lymphocytes by nonprofessional antigen-presenting cells and tumors. *J. Exp. Med.* **205**, 2965–2973 (2008).
56. Joller, N. et al. Cutting edge: TIGIT has T cell-intrinsic inhibitory functions. *J. Immunol. Baltim. Md 1950* **186**, 1338–1342 (2011).
57. Ramsbottom, K. M. et al. Cutting edge: DNAX accessory molecule 1-deficient CD8+ T cells display immunological synapse defects that impair antitumor immunity. *J. Immunol. Baltim. Md 1950* **192**, 553–557 (2014).
58. Shao, Q. et al. TIGIT Induces (CD3+) T cell dysfunction in colorectal cancer by inhibiting glucose metabolism. *Front. Immunol.* **12**, 688961 (2021).
59. Huang, M. et al. The immune checkpoint TIGIT/CD155 promotes the exhaustion of CD8 + T cells in TNBC through glucose metabolic reprogramming mediated by PI3K/AKT/mTOR signaling. *Cell Commun. Signal. CCS* **22**, 35 (2024).
60. Kim, K. et al. Highly efficient RNA-guided base editing in mouse embryos. *Nat. Biotechnol.* **35**, 435–437 (2017).
61. Rees, H. A. et al. Improving the DNA specificity and applicability of base editing through protein engineering and protein delivery. *Nat. Commun.* **8**, 15790 (2017).
62. Manfredi, F. et al. Flow cytometry data mining by cytoChain identifies determinants of exhaustion and stemness in TCR-engineered T cells. *Eur. J. Immunol.* **51**, 1992–2005 (2021).
63. Shoushtari, A. N. & Powell, D. J. Tumor-infiltrating lymphocyte therapy for melanoma and other solid tumors: Looking back, yet moving forward. *Transplant. Cell. Ther.* **31**, S581–S590 (2025).
64. Melenhorst, J. J. et al. Decade-long leukaemia remissions with persistence of CD4+ CAR T cells. *Nature* **602**, 503–509 (2022).
65. Hong, D. S. et al. Autologous T cell therapy for MAGE-A4+ solid cancers in HLA-A*02+ patients: A phase 1 trial. *Nat. Med.* **29**, 104–114 (2023).
66. Commissioner, O. of the. FDA Approves First Gene Therapy to Treat Adults with Metastatic Synovial Sarcoma. *FDA* https://www.fda.gov/news-events/press-announcements/fda-approves-first-gene-therapy-treat-adults-metastatic-synovial-sarcoma (2024).
67. Hong, M., Clubb, J. D. & Chen, Y. Y. Engineering CAR-T cells for next-generation cancer therapy. *Cancer Cell* **38**, 473–488 (2020).
68. Bonini, C. et al. Genome editing in engineered T cells for cancer immunotherapy. *Hum. Gene Ther.* **34**, 853–869 (2023).
69. Spiga, M. et al. Harnessing the tumor microenvironment to boost adoptive T cell therapy with engineered lymphocytes for solid tumors. *Semin. Immunopathol.* **46**, 8 (2024).
70. Corse, E., Gottschalk, R. A. & Allison, J. P. Strength of TCR-peptide/MHC interactions and in vivo T cell responses. *J. Immunol. Baltim. Md 1950* **186**, 5039–5045 (2011).
71. Hasan, M. F. et al. Knockout of the inhibitory receptor TIGIT enhances the antitumor response of ex vivo expanded NK cells and prevents fratricide with therapeutic Fc-active TIGIT antibodies. *J. Immunother. Cancer* **11**, e007502 (2023).
72. Ruella, M. et al. Induction of resistance to chimeric antigen receptor T cell therapy by transduction of a single leukemic B cell. *Nat. Med.* **24**, 1499–1503 (2018).
73. Levine, B. L. et al. Unanswered questions following reports of secondary malignancies after CAR-T cell therapy. *Nat. Med.* **30**, 338–341 (2024).

74. Ozdemirli, M. et al. Indolent CD4+ CAR T-cell lymphoma after cilta-cel CAR T-cell therapy. *N. Engl. J. Med.* **390**, 2074–2082 (2024).
75. Anzalone, A. V., Koblan, L. W. & Liu, D. R. Genome editing with CRISPR-Cas nucleases, base editors, transposases and prime editors. *Nat. Biotechnol.* **38**, 824–844 (2020).
76. Schiroli, G. et al. Precise gene editing preserves hematopoietic stem cell function following transient p53-mediated DNA damage response. *Cell Stem Cell* **24**, 551–565.e8 (2019).
77. Leibowitz, M. L. et al. Chromothripsis as an on-target consequence of CRISPR-Cas9 genome editing. *Nat. Genet.* **53**, 895–905 (2021).
78. Turchiano, G. et al. Quantitative evaluation of chromosomal rearrangements in gene-edited human stem cells by CAST-Seq. *Cell Stem Cell* **28**, 1136–1147.e5 (2021).
79. Tsuchida, C. A. et al. Mitigation of chromosome loss in clinical CRISPR-Cas9-engineered T cells. *Cell* **186**, 4567–4582.e20 (2023).
80. Preece, R. et al. CRISPR-mediated base conversion allows discriminatory depletion of endogenous T cell receptors for enhanced synthetic immunity. *Mol. Ther. Methods Clin. Dev.* **19**, 149–161 (2020).
81. Georgiadis, C. et al. Base-edited CAR T cells for combinational therapy against T cell malignancies. *Leukemia* **35**, 3466–3481 (2021).
82. Yu, Y. et al. Cytosine base editors with minimized unguided DNA and RNA off-target events and high on-target activity. *Nat. Commun.* **11**, 2052 (2020).
83. Doman, J. L., Raguram, A., Newby, G. A. & Liu, D. R. Evaluation and minimization of Cas9-independent off-target DNA editing by cytosine base editors. *Nat. Biotechnol.* **38**, 620–628 (2020).
84. Gaudelli, N. M. et al. Programmable base editing of A•T to G•C in genomic DNA without DNA cleavage. *Nature* **551**, 464–471 (2017).
85. Buchholz, M. et al. Transcriptome analysis of human hepatic and pancreatic stellate cells: organ-specific variations of a common transcriptional phenotype. *J. Mol. Med. Berl. Ger.* **83**, 795–805 (2005).
86. Lowe, A. W. et al. Gene expression patterns in pancreatic tumors, cells and tissues. *PLOS ONE* **2**, e323 (2007).
87. Badea, L., Herlea, V., Dima, S. O., Dumitrascu, T. & Popescu, I. Combined gene expression analysis of whole-tissue and microdissected pancreatic ductal adenocarcinoma identifies genes specifically overexpressed in tumor epithelia. *Hepatogastroenterology* **55**, 2016–2027 (2008).
88. Collisson, E. A. et al. Subtypes of pancreatic ductal adenocarcinoma and their differing responses to therapy. *Nat. Med.* **17**, 500–503 (2011).
89. Goonesekere, N. C. W., Wang, X., Ludwig, L. & Guda, C. A meta analysis of pancreatic microarray datasets yields new targets as cancer genes and biomarkers. *PLOS ONE* **9**, e93046 (2014).
90. Moffitt, R. A. et al. Virtual microdissection identifies distinct tumor- and stroma-specific subtypes of pancreatic ductal adenocarcinoma. *Nat. Genet.* **47**, 1168–1178 (2015).
91. Müller, S. et al. Next-generation sequencing reveals novel differentially regulated mRNAs, lncRNAs, miRNAs, sdRNAs and a piRNA in pancreatic cancer. *Mol. Cancer* **14**, 94 (2015).
92. Bailey, P. et al. Genomic analyses identify molecular subtypes of pancreatic cancer. *Nature* **531**, 47–52 (2016).
93. Mao, Y. et al. RNA sequencing analyses reveal novel differentially expressed genes and pathways in pancreatic cancer. *Oncotarget* **8**, 42537–42547 (2017).
94. Klett, H. et al. Identification and validation of a diagnostic and prognostic multi-gene biomarker panel for pancreatic ductal adenocarcinoma. *Front. Genet.* **9**, 108 (2018).
95. Tang, Y., Zhang, Z., Tang, Y., Chen, X. & Zhou, J. Identification of potential target genes in pancreatic ductal adenocarcinoma by bioinformatics analysis. *Oncol. Lett.* **16**, 2453–2461 (2018).
96. Zhao, L., Zhao, H. & Yan, H. Gene expression profiling of 1200 pancreatic ductal adenocarcinoma reveals novel subtypes. *BMC Cancer* **18**, 603 (2018).
97. Maurer, C. et al. Experimental microdissection enables functional harmonisation of pancreatic cancer subtypes. *Gut* **68**, 1034–1043 (2019).
98. Peng, J. et al. Single-cell RNA-seq highlights intra-tumoral heterogeneity and malignant progression in pancreatic ductal adenocarcinoma. *Cell Res.* **29**, 725–738 (2019).
99. Lin, W. et al. Single-cell transcriptome analysis of tumor and stromal compartments of pancreatic ductal adenocarcinoma primary tumors and metastatic lesions. *Genome Med* **12**, 80 (2020).
100. Bassani-Sternberg, M. et al. A phase Ib study of the combination of personalized autologous dendritic cell vaccine, aspirin, and standard of care adjuvant chemotherapy followed by nivolumab for resected pancreatic adenocarcinoma-A proof of antigen discovery feasibility in three patients. *Front. Immunol.* **10**, 1832 (2019).
101. Antwi, K. et al. Proteomic identification of an MHC-binding peptidome from pancreas and breast cancer cell lines. *Mol. Immunol.* **46**, 2931–2937 (2009).
102. Choi, Y. J. et al. EpCAM peptide-primed dendritic cell vaccination confers significant anti-tumor immunity in hepatocellular carcinoma cells. *PLOS ONE* **13**, e0190638 (2018).
103. Stromnes, I. M. et al. T cells engineered against a native antigen can surmount immunologic and physical barriers to treat pancreatic ductal adenocarcinoma. *Cancer Cell* **28**, 638–652 (2015).
104. Yokokawa, J. et al. Identification of novel human CTL epitopes and their agonist epitopes of mesothelin. *Clin. Cancer Res. J. Am. Assoc. Cancer Res.* **11**, 6342–6351 (2005).
105. Duan, Z.-L. et al. Two novel squamous cell carcinoma antigen-derived HLA-A*0201-binding peptides induce in vitro and in vivo CD8+ cytotoxic T lymphocyte responses. *Int. J. Oncol.* **42**, 1482–1492 (2013).
106. Berinstein, N. L. et al. First-in-man application of a novel therapeutic cancer vaccine formulation with the capacity to induce multi-functional T cell responses in ovarian, breast and prostate cancer patients. *J. Transl. Med.* **10**, 156 (2012).
107. Poon, E. C. C. Assessment of TWIST1 as an immunotherapeutic target of cancer. Doctoral dissertation. Institute of Child Health, University College London, (2011).
108. Rongcun, Y. et al. Identification of new HER2/neu-derived peptide epitopes that can elicit specific CTL against autologous and allogeneic carcinomas and melanomas. *J. Immunol. Baltim. Md 1950* **163**, 1037–1044 (1999).
109. Scardino, A. et al. Identification of HER-2/neu immunogenic epitopes presented by renal cell carcinoma and other human epithelial tumors. *Eur. J. Immunol.* **31**, 3261–3270 (2001).
110. Okugawa, T. et al. A novel human HER2-derived peptide homologous to the mouse K(d)-restricted tumor rejection antigen can induce HLA-A24-restricted cytotoxic T lymphocytes in ovarian cancer patients and healthy individuals. *Eur. J. Immunol.* **30**, 3338–3346 (2000).
111. Kubuschok, B. et al. Naturally occurring T-cell response against mutated p21 ras oncoprotein in pancreatic cancer. *Clin. Cancer Res. J. Am. Assoc. Cancer Res.* **12**, 1365–1372 (2006).
112. Schirle, M. et al. Identification of tumor-associated MHC class I ligands by a novel T cell-independent approach. *Eur. J. Immunol.* **30**, 2216–2225 (2000).
113. Tran, E. et al. Immunogenicity of somatic mutations in human gastrointestinal cancers. *Science* **350**, 1387–1390 (2015).
114. Bolotin, D. A. et al. Next generation sequencing for TCR repertoire profiling: platform-specific features and correction algorithms. *Eur. J. Immunol.* **42**, 3073–3083 (2012).

115. Ruggiero, E. et al. High-resolution analysis of the human T-cell receptor repertoire. *Nat. Commun.* **6**, 8081 (2015).
116. Klempner, S. J. et al. DKN-01 in combination with tislelizumab and chemotherapy as first-line therapy in advanced gastric or gastroesophageal junction adenocarcinoma: DisTinGuish. *J. Clin. Oncol.* **43**, 339–349 (2025).
117. Kluesner, M. G. et al. EditR: A method to quantify base editing from Sanger sequencing. *CRISPR J.* **1**, 239–250 (2018).
118. Amendola, M., Venneri, M. A., Biffi, A., Vigna, E. & Naldini, L. Coordinate dual-gene transgenesis by lentiviral vectors carrying synthetic bidirectional promoters. *Nat. Biotechnol.* **23**, 108–116 (2005).
119. Lévy, C. et al. Lentiviral vectors displaying modified measles virus gp overcome pre-existing immunity in in vivo-like transduction of human T and B cells. *Mol. Ther. J. Am. Soc. Gene Ther.* **20**, 1699–1712 (2012).
120. Tang, R. et al. Enhanced T cell glucose uptake is associated with progression of beta-cell function in type 1 diabetes. *Front. Immunol.* **13**, 897047 (2022).
121. Vlachogiannis, G. et al. Patient-derived organoids model treatment response of metastatic gastrointestinal cancers. *Science* **359**, 920 (2018).
122. Driehuis, E., Kretzschmar, K. & Clevers, H. Establishment of patient-derived cancer organoids for drug-screening applications. *Nat. Protoc.* **15**, 3380–3409 (2020).
123. Cattaneo, C. M. et al. Tumor organoid-T-cell coculture systems. *Nat. Protoc.* **15**, 15–39 (2020).

Acknowledgements

M.S. conducted this study in partial fulfillment of her International Ph.D. Course in Molecular Medicine at San Raffaele University, Milan. We thank all the members of the AIRC 5×1000 (A5M) program project entitled'Advanced immune gene and cell therapies for liver metastases'. We thank the IRCCS San Raffaele Hospital Advanced Light and Electron Microscopy BioImaging Center (ALEMBIC), Cesare Covino for providing help with the Incucyte data analysis and Desiree Zambroni for the analysis of immune synapses. We thank Stefano Grassi from the Pathology Unit of the IRCCS San Raffaele Scientific Institute for immunohistochemical analyses on human samples. We thank Amleto Fiocchi, from the animal histopatology unit of the IRCCS San Raffaele Scientific Institute, and Martina Rocchi from the GLP Test Facility of SR-TIGET, for immunohistochemical analyses on mouse samples. We thank Raffaella Di Micco and Teresa Tavella of SR-TIGET for sharing senescence gene signatures. We also thank Luca Vago, Paolo Dellabona, and Monica Casucci from the IRCCS San Raffaele Scientific Institute for scientific discussion. Figures were created using Adobe Illustrator (Adobe Inc 2019) and Servier Medical Art templates, which are licensed under a Creative Commons Attribution 3.0 Unported License. This work was supported by Associazione Italiana per la Ricerca sul Cancro (AIRC 5 per Mille 22737 and AIRC-IG 18458), Italian Ministry of Research and University (PRIN 2017WC8499, 2022SLL3YZ), Italian Ministry of Health (Research project on CAR-T cells for hematological malignancies and solid tumors and RF-2019–12370243) EU (T2Evolve, Join4ATMP) RF-2021-12373598 "Uncover and overcome senescence and dysfunction of genetically engineered T lymphocytes for cancer immunotherapy" awarded to C.Bo, and by two AIRC Postdoctoral Fellowships awarded to M.S (29911-2023) and A.Pot (29914-2023).

Author contributions

M.S. and A.Pot. designed the study, performed the experiments, analysed and interpreted data and wrote the manuscript. Z.M. performed the experiments and interpreted the data. S.B performed bioinformatic analyses of WES and NGS data. B.C performed in vivo experiments. L.C, A.A, N.M, C.I, L.S.S, A.U, A.G participated in experiments. C.D., M.P., and F.S. performed and analyzed immunohistochemistry experiments. L.P. performed ultrasound imaging analyses. C.Ba performed bioinformatic analyses of RNAseq data. D.A helped with flow cytometry data. G.G and O.B participated in CRC organoids preparation for in vitro and in vivo experiments.M.Rei, H.A. and A.Poc participated in designing PDAC in vivo experiments and data discussion. M.F. and S.F. supported T-cell engineering and safety analyses.G.DL managed patients' samples. G.T., G.S., MP.P., A.M, R.O., G.B., M.Ren, S.C., M.F., and L.N. participated in data discussion and interpretation. E.R designed and supervised the study, performed TCR sequencing and participated in data discussion and interpretation of results. C.Bo designed and supervised experiments, discussed data, interpreted results, and wrote the manuscript and is the guarantor of this study.

Competing interests

CBo has been member of Advisory Board and Consultant for Intellia, TxCell, Novartis, GSK, Allogene, Kite/Gilead, Kiadis, Evir, Janssen, Genyo, Epsilen, and received research support from Intellia Therapeutics. MS, AP, ER, and CBo are inventors in the patent WO2025/003481 including TCRs and sgRNAs employed in this work. AP, ZM, ER, CBo are inventors on different patents on cancer immunotherapy and genetic engineering. L.N. is founder of, quota holder and consultant for GeneSpire and Epsilen Bio/Chroma Medicine. All other authors declare no competing interests.

Additional information

Supplementary information The online version contains supplementary material available at https://doi.org/10.1038/s41467-025-67263-w.

Correspondence and requests for materials should be addressed to Chiara Bonini.

Peer review information *Nature Communications* thanks Prasad Adusumilli, Marco Donia and the other, anonymous, reviewer(s) for their contribution to the peer review of this work. A peer review file is available.

[1]Experimental hematology Unit, Division of Immunology, Transplantation and Infectious Diseases, IRCCS San Raffaele Scientific Institute, Milan, Italy. [2]San Raffaele-Telethon Institute for Gene Therapy (SR-Tiget), IRCSS San Raffaele Scientific Institute, Milan, Italy. [3]Preclinical Imaging, Experimental Imaging Centre, IRCCS San Raffaele Scientific Institute, Milan, Italy. [4]Pathology Unit, IRCCS San Raffaele Scientific Institute, Milan, Italy. [5]Vita-Salute San Raffaele University, Milan, Italy. [6]Center for Omics Sciences, IRCCS San Raffaele Scientific Institute, Milan, Italy. [7]Functional Genomics of Cancer Unit, IRCCS San Raffaele Scientific Institute, Milan, Italy. [8]Translational Pancreatic Cancer Research Center, Medical Clinic and Polyclinic II, Klinikum rechts der Isar, Technische Universität München, Munich, Germany. [9]Department of Gastroenterology, Internal Medicine II, Klinikum rechts der Isar, Technical University of Munich (TUM), Munich, Germany. [10]Lymphocyte activation Unit, Division of Immunology, Transplantation and Infectious Diseases, IRCCS San Raffaele Scientific Institute, Milan, Italy. [11]Experimental hepatology, Division of Immunology, Transplantation and Infectious Diseases, IRCCS San Raffaele Scientific Institute, Milan, Italy. [12]Pancreatic Surgery and Transplantation Unit, Pancreas Translational and Clinical Research Centre, IRCCS San Raffaele Scientific Institute, Milan, Italy. [13]Tumor immunology Unit, Division of Immunology, Transplantation and Infectious Diseases, IRCCS San Raffaele Scientific Institute, Milan, Italy. [14]Medical Oncology Unit, Pancreas Translational and Clinical Research Centre, IRCCS San Raffaele Scientific Institute, Milan, Italy. [15]These authors contributed equally: Martina Spiga, Alessia Potenza. [16]These authors jointly supervised this work: Eliana Ruggiero, Chiara Bonini.
✉e-mail: bonini.chiara@hsr.it